



LAWRENCE
LIVERMORE
NATIONAL
LABORATORY

LLNL-TR-417672

Compact Gamma-ray Source Technology Development Study

S. G. Anderson, D. J. Gibson, B. Rusnak

October 7, 2009

Disclaimer

This document was prepared as an account of work sponsored by an agency of the United States government. Neither the United States government nor Lawrence Livermore National Security, LLC, nor any of their employees makes any warranty, expressed or implied, or assumes any legal liability or responsibility for the accuracy, completeness, or usefulness of any information, apparatus, product, or process disclosed, or represents that its use would not infringe privately owned rights. Reference herein to any specific commercial product, process, or service by trade name, trademark, manufacturer, or otherwise does not necessarily constitute or imply its endorsement, recommendation, or favoring by the United States government or Lawrence Livermore National Security, LLC. The views and opinions of authors expressed herein do not necessarily state or reflect those of the United States government or Lawrence Livermore National Security, LLC, and shall not be used for advertising or product endorsement purposes.

This work performed under the auspices of the U.S. Department of Energy by Lawrence Livermore National Laboratory under Contract DE-AC52-07NA27344.

Compact Gamma-ray Source Technology Development Study

Scott G. Anderson, David J. Gibson, Brian Rusnak

September 24, 2009

This study focuses on the applicability of current accelerator and laser technologies to the construction of compact, narrow bandwidth, gamma-ray sources for DHS missions in illicit materials detection. It also identifies research and development areas in which advancement will directly benefit these light sources.

In particular, we review the physics of Compton scattering based light sources and emphasize the source properties most important to Nuclear Resonance Fluorescence (NRF) applications of interest. The influences of laser and electron beam properties on the light source are examined in order to evaluate the utility of different technologies for this application.

Applicable bulk and fiber-based laser systems and laser recirculation technologies are discussed and Radio Frequency (RF) Linear Accelerator (linac) technologies are examined to determine the optimal frequency and pulse formats achievable.

1 Accelerator Considerations

In this section we evaluate how accelerator technology can be optimally combined with high power laser technology to create compact, quasi-mono-energetic photon beams in the x-ray range via Compton backscattering laser light off of 150-300 MeV electrons. This report summarizes performance issues in electron RF accelerator technology in how it can best be utilized to achieve compact photon sources.

Common to all of the proposed NRF applications is the need for high average photon flux at a specified energy (i.e., to maximize $N_\gamma/eV/sec$ at the NRF resonances line) while concurrently minimizing background noise from off-resonance radiation. For the Compton source, these requirements motivate the use of small laser and electron beam sizes, σ_x , at the interaction point (IP) to increase flux, yet maintain a small normalized beam divergence, $\gamma\sigma_{x'}$, to decrease the bandwidth of the γ -rays.

The effect of electron beam divergence on source bandwidth can be seen through the expression for scattered photon energy in the Thomson limit (where $\gamma E_L \ll m_e c^2$),

$$E_\gamma \approx 2\gamma^2 E_L \frac{1 + \cos \phi}{1 + \gamma^2 \theta^2}, \quad (1)$$

where ϕ is the angle between electron and incident photon, defined such that $\phi = 0$ for a head-on collision, and θ is the observation angle with respect to the electron direction. In addition to the Compton electron recoil effect, this formula ignores nonlinear laser field effects, which will be discussed in detail below. If we consider the head-on collision geometry, then the angles

are defined with respect to the electron beam axis, and $\phi = \theta$ is the small angle made by an electron with respect to the beam axis due to non-zero emittance. Then Eq. 1 can be expanded to give

$$\left. \frac{\Delta E_y}{E_y} \right|_{\text{on-axis}} = \frac{\Delta E_L}{E_L} + \frac{2\Delta y}{y} - y^2 \Delta \theta^2. \quad (2)$$

In a more rigorous analysis [1], it has been shown that, in summing over the beam, the terms in Eq. 2 add in quadrature to give the γ -ray source bandwidth. The final term corresponds with the square of the normalized beam divergence, or $\varepsilon_n^2/\sigma_x^2$. Because this expression involves the *normalized* emittance, a high brightness beam is required to efficiently scatter photons while maintaining a narrow bandwidth. The total number of γ -ray photons produced per pulse, $N_{\gamma, \text{pulse}}$, depends on the intensities of the overlapping electron and laser beams as they interact. Assuming Gaussian laser and electron beam profiles, and that the beam dimensions do not change significantly during the interaction, the number of γ -rays produced is

$$N_{\gamma, \text{pulse}} = \frac{N_e N_L \sigma_T}{2\pi (\sigma_e^2 + \sigma_L^2)}, \quad (3)$$

where N_e and N_L are the number of input electrons and photons, respectively, σ_e and σ_L are the beam rms sizes, and σ_T is the total Thomson cross section.

Using Eqns. 2 and 3, and assuming the laser and electron beam spot sizes are matched, and that the emittance term in Eq. 2 is dominant, we can see the dependence of the on-resonance, average photon flux on electron beam parameters:

$$N_{\gamma}/\text{eV}/\text{sec} \propto \frac{N_{\gamma, \text{pulse}} f_{\text{rep}}}{\Delta E_y/E_y} \propto \frac{N_e f_{\text{rep}}}{\sigma_e^2} \cdot \frac{\sigma_e^2}{\varepsilon_n^2} = \frac{N_e f_{\text{rep}}}{\varepsilon_n^2}, \quad (4)$$

where f_{rep} is the pulse repetition frequency. Thus, the quantity to be maximized in the accelerator design is the average beam current over the square of the normalized emittance. Some care must be taken to ensure that the emittance term in Eq. 2 is in fact dominant. As will be shown below, minimizing emittance in a particular accelerator design will place requirements on the energy spread, bunch length, and charge that must be attained.

Tolerance to electron beam pointing jitter at the IP can also be evaluated using Eq. 2. Over multiple shots, errors in electron beam pointing will increase the effective beam divergence and therefore increase source bandwidth:

$$\Delta \theta_{\text{eff}}^2 = \sigma_{x'}^2 + \theta_{\text{jitter}, \text{rms}}^2 \quad (5)$$

In the accelerator designs to be considered, the stability criterion: $\theta_{\text{jitter}, \text{rms}} < 0.2\sigma_{x'}$, needs to be achievable to keep the effect of pointing jitter negligible. A similar constraint on position jitter must be chosen to minimize growth of the effective spot size at the IP.

1.1 Background

Particle accelerators as scientific instruments have been around for nearly a century, primarily for producing high energy particle beams. Over that time, the specific need for sub-atomic

particles at a given energy has driven the performance requirements and costs of the accelerator, and usually particles energies are desired to push the frontiers of physics at the highest energy that the budget, schedule, and space allow. As accelerator physics understanding and technology improve, larger and higher energy machines can and have been built to keep the field moving forward. As part of this process, accelerator evolution is typically incremental in nature, building piecewise upon and maximally leveraging previous hardware, experience, and capability. Given the scale, cost, and complexity of most nuclear and high energy physics machines, this business model works reasonably well as it reduces risk and cost of new proposed designs that are pushing the energy frontier. The main downside of this approach is it can artificially constrain the design process if the technical objectives are significantly different than what has been done previously.

As recent national security needs have evolved in the past decade, the desire to leverage existing capabilities in accelerator technology to economize the process is at odds with achieving optimal performance, especially for highly compact configurations. The design space for accelerator technology to produce particle beams is complicated and highly interdependent, and is all the more so when it is additionally constrained by compactness or intensity considerations.

1.2 Accelerator Technology

There are a large number of technologies available for accelerating charged particles. As the application here requires pulsed, high-quality electron beams in the 150-300 MeV energy range, RF linac technology was looked at exclusively. While circular machines are certainly viable contenders for producing bunched electron beams in this energy range, they are not readily scalable for compactness due to the bending magnets and fields needed to achieve circularity.

The choices for linear RF accelerator technology spans travelling-wave (TW) and standing-wave (SW) normal conducting linacs as well as superconducting RF (SRF) linacs. TW linacs are a specialized form of linear accelerator where a very high power RF pulse propagates down a disk-loaded waveguide structure that slows the phase velocity of the wave to nominally match the particle velocity as it moves down the RF structure. The beam takes energy out of the RF wave and is accelerated, and the leftover RF energy is dumped in a resistive load at the end of the structure. This type of linac has been built and operated at numerous facilities around the world, e.g., SLAC, IHEP-Beijing, LLNL, BNL, and the Naval Postgraduate School, and has achieved very high acceleration gradients in application. The main benefit of this type of linac is it operates at high frequency (3-40 GHz), which results in low cavity Q values and short fill and decay times for cavity fields. This enables running with very short RF pulse lengths, which allows for effectively taking advantage of the heat capacity “stored” in the cavity walls — the fields are established, accelerate the beam, and decay away before the temperature rise in the cavity is so high as to lose phase lock due to cavity detuning. The temperature rise in a structure as a function of pulse length for different frequencies as evaluated by Wilson [2] is shown in Fig. 1, as an example of this effect. The main technical challenge with TW linacs is associated with the very high power RF pulse needed to set up the acceleration fields in the cavity. As very high gradient applications require significantly more power than a round-beam klystron can deliver (60-70 MW/pulse) due to fundamental physics limitations in the klystron tube, pulse stacking technology is often employed to combine RF pulses to achieve the 200-300 MW/pulse required to drive the structure at the highest gradients. SW linacs are

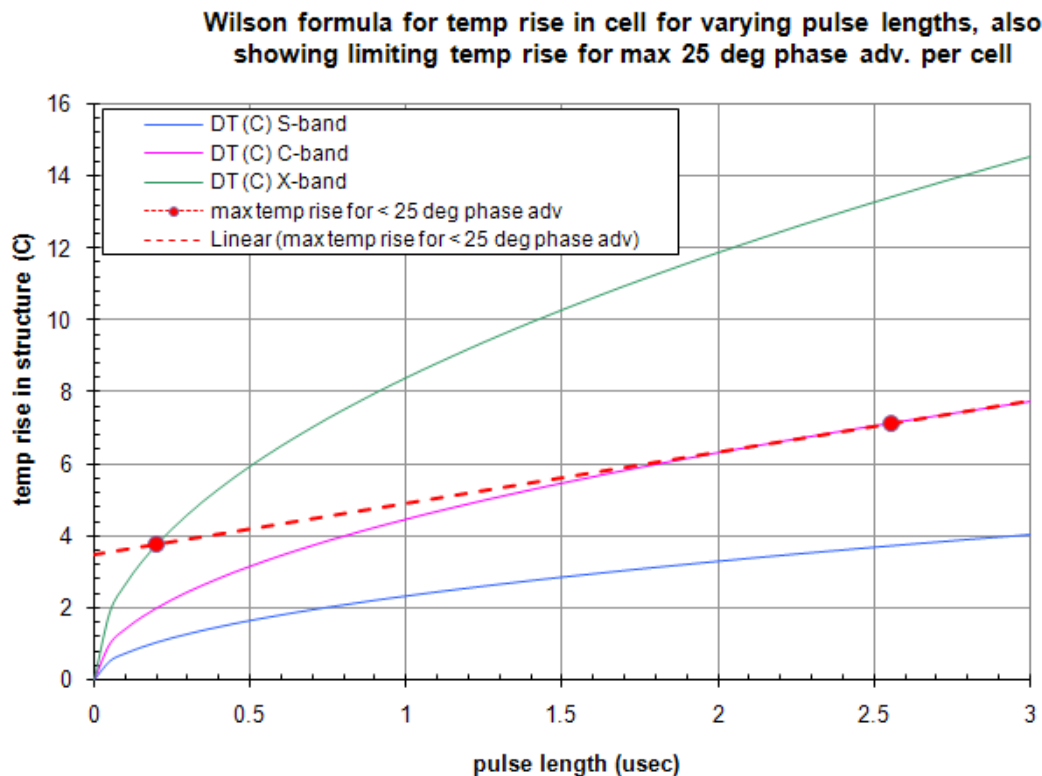


Figure 1: Plot of the calculated temperature rise per RF pulse as a function of pulse length for three frequencies based on Wilson. The dashed line shows the maximum temperature rise, and thus the maximum pulse length, to keep phase excursions due to thermal-expansion-based detuning below 25 degrees in phase. Curves are for 62.5, 72.8, and 84.8 MV/m accelerating gradient for S, C, and X band respectively.

fundamentally different than TW linacs in that they take advantage of RF fields built up as the superposition of reflecting travelling waves that create standing waves in the cavity. For linacs of this type, lower RF power is needed since the cavity generates higher fields due to higher cavity Q associated with the greater volume of a cavity at lower frequency. The main challenge in this linac type is the lower frequency and higher Q of the structure means it can only be efficiently run at longer pulse lengths and higher repetition rates, and removing the deposited heat in the walls ultimately limits performance.

SRF linacs are a specialized version of a SW linac, in that the cavity walls are made of niobium metal that goes superconducting at 9.2 K. With surface resistances a factor of 10^4 – 10^5 less than copper, the cavity Q is subsequently at 10^9 – 10^{10} . SRF technology offers a high performance solution to the heat dissipation problem that limits SW normal conducting linacs, and the efficiency gains made by the enormous increase in Q value actually more than compensate the added power needed for cryogenic cooling to 2 or 4 K. In large machines, even the capital cost of the refrigerator is offset by the reduced RF power requirements.

For all linacs, the primary goal is to accelerate particles with maximum electrical efficiency.

For large normal-conducting machines, this is often concurrent with achieving the highest acceleration gradient, E_a , in the structure as possible. The reasoning is, higher gradients result in shorter overall accelerator lengths, which reduce the overall tunnel and all associated utility infrastructure and capital cost. This is indeed the case where the extent of active acceleration structures dominates the overall linac architecture. However, in the case of smaller, lower-energy machines where the injection and beam transport lines are of comparable spatial extent as the acceleration structures, the gains realized by higher gradient are much reduced. As will be seen, the extent of the “drift” sections in an accelerator needed for beam diagnostics, focusing magnets, vacuum pumping, and beam phase space manipulation and clean up can have a major impact of machine design regarding compactness.

1.3 The Pursuit of Gradient in Normal Conducting RF Structures

Operating RF structures at high accelerating gradient has always posed numerous technical challenges. As RF power levels being fed into a structure are increased, at some point RF conditioning begins that results in vacuum activity and x-rays. The RF fields are producing free electrons that get accelerated to moderate energies and hit the walls, liberating secondary electrons and driving off absorbed gases on the surface. This processing activity will abate after time as emitter sites are “cleaned up” by evaporation or destruction, and the power can be increased further to condition the cavity surface to higher fields. At some point, the cavity will catastrophically break down via an arc, and the conditioning degree of the cavity cannot be improved (and may actually be deteriorated). This level of breakdown is the limit for the acceleration field gradient that can be sustained in a given cavity, and operating accelerators run below the breakdown limit to ensure stable, reliable operation.

The nature of the breakdown limit in RF cavities turns out to be a very complicated phenomenology, and has been studied for at least four decades. The interaction of RF electromagnetic energy with micron-scale particulate matter, surface layers of oxides, absorbed monolayers of water, surface contaminants, and vacuum make for a very complicated surface physics problem. The earliest published work for explaining RF breakdown comes from Kilpatrick in 1957 [3], where he proposed a model of electron-ion-surface interaction that accounts for ion energy related to transit time and phase relative to the RF fields and has provided a basis for evaluating breakdown performance in RF cavities ever since.

The Kilpatrick model was developed based on observations of field breakdown across two RF electrodes at 200 MHz, as well as RF and DC data from other sources, circa 1957. As expanded upon by Wang [4], the Kilpatrick criterion rendered in frequency and electric field is given by

$$f = 1.64E^2 e^{\left(\frac{-8.5}{E}\right)}, \quad (6)$$

where f is in MHz and E is the maximum (peak) electric field in MV/m. Since for high electric fields ($E \gg 8.5$) the exponential approaches 1, the nominal Kilpatrick scaling of field with frequency goes as

$$E \sim f^{\frac{1}{2}}. \quad (7)$$

Since this work was published, decades of development on RF accelerators has amply shown that the above criterion and related scaling do not adequately capture the complexity of the problem and at best serves as a guideline for common comparison. Data on numerous

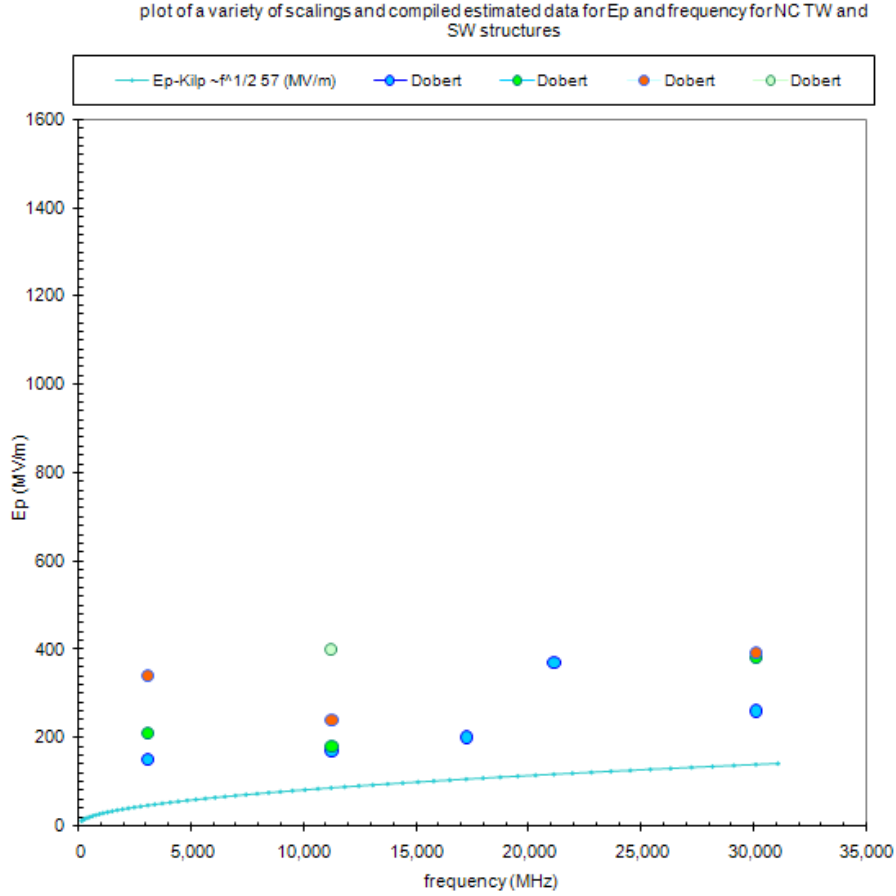


Figure 2: Plot showing peak electric field in mostly TW accelerating cavities as a function of frequency spanning the last 27 years, compared to the Kilpatrick criterion (blue line). For these structures, typically E_a approximately equals $3 \cdot E_p$.

machines has shown overall field performance for RF cavities to be far above the expectation values of the criterion at a given frequency, with greater than expected improvements being observed at increasingly higher frequency. Spread in the data as a function of frequency also challenged the validity of the scaling model. As shown in Fig. 2 below, data for testing on mostly travelling-wave structures from 2.854 to 30 GHz spanning $\sim 1980 - 2002$ is plotted against the above criterion and the disparity with the model is obvious.

There are a number of potential reasons the data outperformed the model as proposed. The first and most obvious factor is vacuum pumping technology has improved dramatically in the last 40 years. Up to 1957, most vacuum pumping systems were oil diffusion and rotary vane backing pumps that resulted in backstreaming oil residues on interior surfaces. Even if ion pumps were used that worked at very low pressures, the systems would still need to be initially evacuated with an oil diffusion pumped system. As even Kilpatrick points out in his paper “if there are small traces of oil on the electrodes, the exponential coefficient is very large, and a deluge of sparks occurs above the threshold.” It seems exceedingly likely that surface

analysis techniques in the 1950's for detecting oil on surfaces were not sufficiently accurate to determine a surface to be oil-free as can be done today, and it is probable that much of the observed data could be attributed to then undetected surface contamination. Indeed, the entire field of contamination control (and even the transistor) had not yet come of age, let alone the vast knowledge, tool, and technology infrastructure base that came with the development of microelectronics.

Another factor mentioned by Wang is the criterion developed by Kilpatrick was not meant to model breakdown in accelerators, which have a variety of cavity shapes and largely varying degrees of E and H field overlap. Special “spark gap” testing equipment, or lower frequency RF cavities often have high degrees of physical separation between oscillating E and H field regions, where more modern, higher frequency cavities see a much larger degree of field overlap. As different particles respond differently to RF fields, e.g., dielectric “dust” may have a high loss tangent and couple to the E field, where metallic particles will be Ohmically heated by the H fields driving currents on the particle, the extent of field overlap is an open question. The presence of magnetic fields can also lead to lower onsets of breakdown, and can prolong field emitted electron lifetimes in the form of multipacting.

Advances in how cavities are RF processed also contributes. As today's cavities run at much higher RF power, and much more sophisticated techniques exist for safely conditioning a cavity to achieve high field operation, it is not clear that what Kilpatrick was calling a “spark” is now something considered to be part of the normal conditioning process. Finally, Kilpatrick only had very limited data at 2.854 GHz, and this was the highest frequency data he had available. As most of the frequency scaling work being looked at relative to Compton sources is at and above this frequency, the relevance of this model extrapolated strains its validity further still.

A perhaps more interesting, and speculative, assessment is offered as to how the evolution of the Kilpatrick model, test results, and ongoing research may have painted an overly optimistic picture of the scaling of field performance related to increasing frequency. As accelerator technology “boomed” in the 1960's to 1970's with the building of the Stanford Linear Accelerator, LAMPF at Los Alamos, the AGS booster and 200 MeV linac at BNL, and the Fermilab main ring and booster to name but a few large projects, data quickly amassed that showed much higher field performance than predicted by Kilpatrick, and much of this data was at operating frequencies much higher than what was used originally in the study.

It seems possible, based on the evolution of models over the past 25 years, that the combination of improved performance (presumed largely due to vacuum technology) and higher frequency encouraged a degree of “nonlinear optimism” with regard to the benefits of going to higher frequency in achieving higher gradient. Building upon Fig. 2, Fig. 3 shows a number of scalings of peak electric field as a function of gradient from different researchers at different times along with the individual data compilations and the average of those compilations.

A number of things are striking about these scalings compared to the data. The first is the overall trend of empirically-based models to become more conservative with time. The orange curve is a model based on data compiled circa 1989 by Wang and Loew [5]. It shows a $\sim f^{1/2}$ scaling consistent with their compiled data. Specifically, they proposed the following scaling law

$$Ep = 195 [f \text{ (GHz)}]^{1/2} . \quad (8)$$

After eight years of work and additional data [6], the same researchers proposed the model be

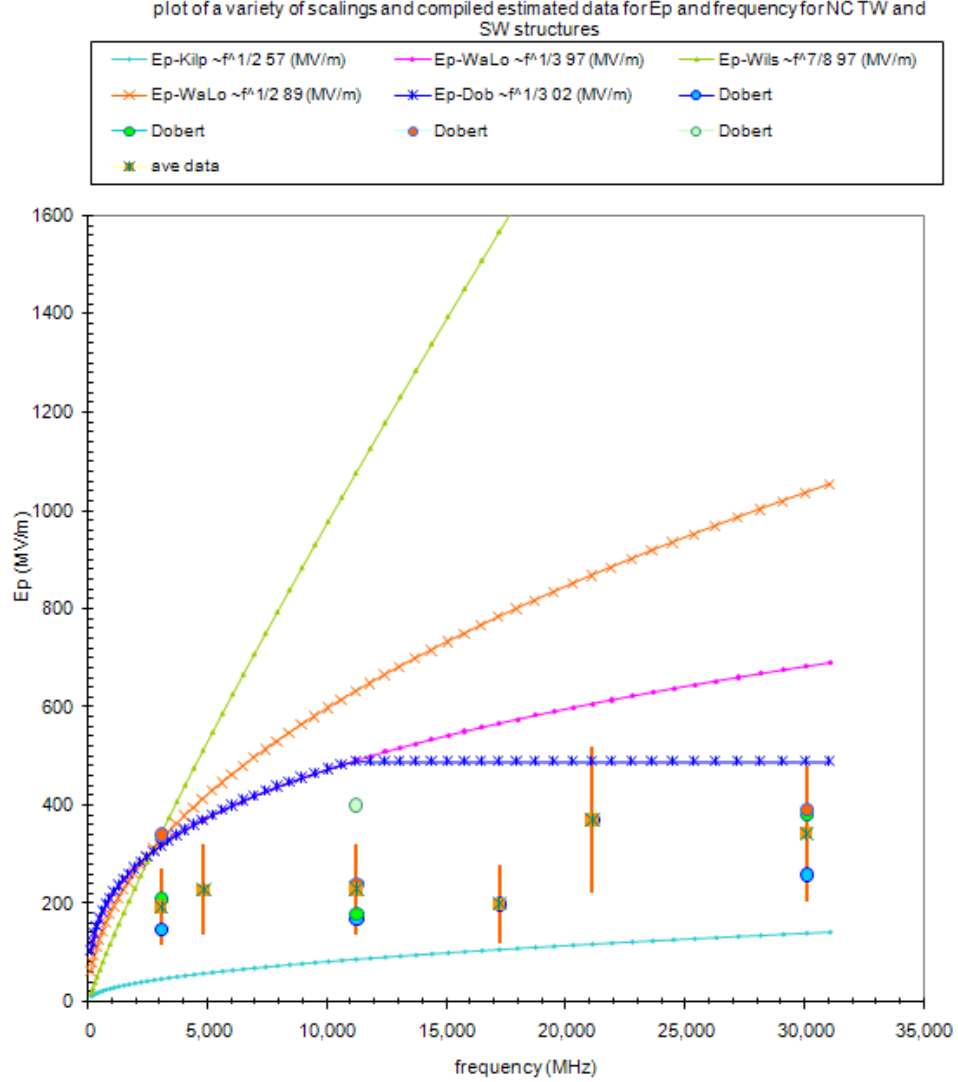


Figure 3: Plot showing a variety of scalings for peak electric field as a function of frequency compared to compiled data and averaged values of compiled data (orange data points with error bars).

revised as shown below and as the magenta curve on Fig. 3

$$E_p = 220 [f \text{ (GHz)}]^{1/3}. \quad (9)$$

This revised empirical model shows a decreased benefit in going to higher gradient. In contrast to this, Wilson proposed in the same year [2] an alternative scaling that couples a plasma-physics-based discharge with a pulse length effect to obtain the scaling represented by the green curve on Fig. 3

$$E_p = 130 [f \text{ (GHz)}]^{7/8}. \quad (10)$$

The significance of this dramatically different scaling is that by 1997, a full 40 years after Kilpatrick's original work on the subject, innovative work was being done in an attempt to capture the complexity of RF breakdown process in cavities that included pulse-length dependence effects.

The final blue curve on Fig. 3 is a modification of the Wang-Loew $\sim f^{1/3}$ scaling model proposed by Döbert in 2002 [7] with a cap at ~ 11 GHz that suggests field performance is flat above this frequency.

The other notable feature of all the proposed models is their consistency at 2.854 GHz, where the majority of the data lie due to the operation of the Stanford Linear Accelerator, compared to the wide inconsistency in their prediction of performance at 10-20 GHz. This is not unexpected, as the majority of models are empirically based, but it does highlight the situation rather well – after 50 years of research, there is still no comprehensive physics model that sufficiently captures breakdown phenomenology in RF accelerating cavities to enable accurate extrapolation above 2-3 GHz without experimental verification.

Fortunately, the lack of robust physics-based models does not diminish the value the research. Sufficient data based on more modern vacuum and diagnostic technology has been collected over the past 20 years, and can provide for pure empirical fits to help bound what are reasonable expectations for performance gains in gradient as a function of frequency. By applying a simple power fit to averages of published data spanning 2.854 – 30 GHz, a $\sim f^{2/9}$ is obtained, and is shown by the dashed orange line in Fig. 4, with the fit as

$$Ep = 32.463 [f \text{ (GHz)}]^{2/9}. \quad (11)$$

While there is ultimately no physics model in the scaling as it is only a power fit of the data, it is still useful over the frequency range shown because sufficient data has been collected over the past 20 years to give confidence in the fit. Using this scaling, there is a predicted potential 36% improvement in gradient going from 2.854 to 11.424 GHz.

1.4 The Pursuit of Gradient in Superconducting RF Structures

Research on superconducting RF (SRF) structures in the past 40 years has also led to a wealth of data that can be used to gain insight into gradients in cavities. Superconducting structures, by virtue of their superconducting cavity walls, have very low RF loss, typically measured in 10's of nano-Ohms. The very high Q values for these cavities at $10^9 - 10^{10}$ make them ideally suited for high repetition rate operation, extending up to continuous wave (CW). In terms of making a compact Compton Backscatter Machine, SRF technology would be useful for achieving very high average intensities of Compton beams, provided high average power laser technology can be developed that can match the accelerator output. As shown in Figure 4 below, the gradients achievable in SRF cavities is below what can be obtained in the highest gradient normal conducting travelling wave cavities, but is still much higher than high duty factor (~ 5 -100%) normal conducting standing wave systems.

Interestingly, a power fit of the SRF data shows an $\sim f^{1/2}$ that is consistent with the Kilpatrick model. It is believed the ion mobility model is applicable at these lower frequency ranges, but that other processes start to dominate at higher frequencies and perhaps gradients as well.

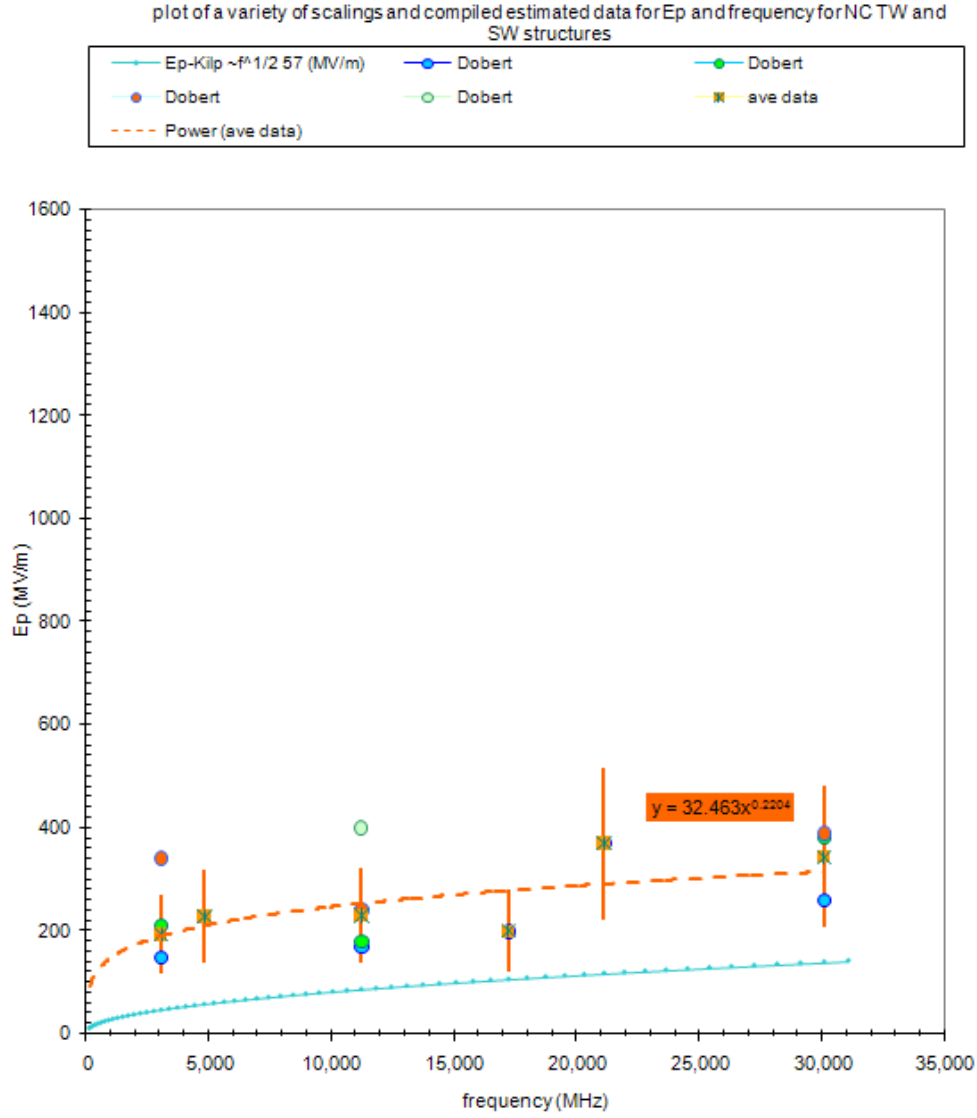


Figure 4: Plot of a power fit (dashed orange line) of the averaged compiled data at each frequency.

Operating SRF structures at higher frequencies than ~ 3 GHz has rapidly diminishing benefit as the Bardeen-Cooper-Schrieffer (BCS) resistance of the superconductor increases as $\sim f^2$, and the cryogenic losses become problematic. Fig. 5 shows a plot of the surface resistance for normal conducting copper and superconducting niobium at 2 K as a function of frequency.

1.5 Influence of Gradient and Frequency on Compactness

In order to make an accelerator that can deliver beam at a specific energy requires applying a broad range of beam and RF structure physics considerations with engineering constraints for

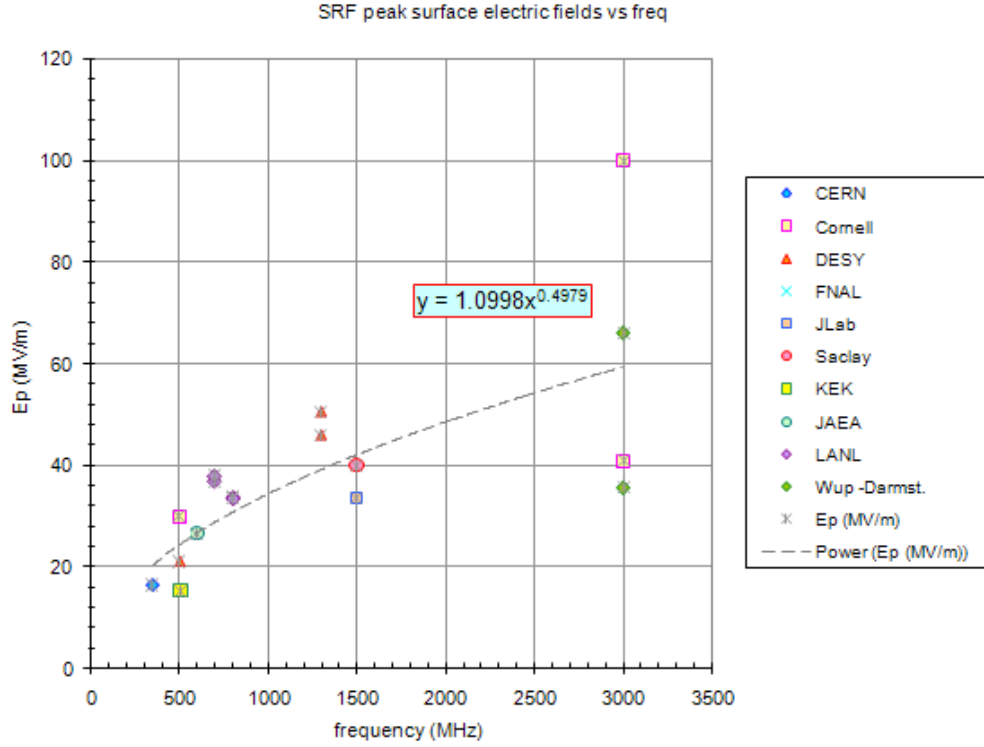


Figure 5: Peak surface field performance data as a function of frequency for superconducting RF cavities.

mechanical robustness, vacuum, and thermal management. To design the same accelerator to be as compact as possible requires pushing all performance metrics to their limits while still abiding the constraints imposed by cavity physics. As gradient is an obvious performance parameter that couples accelerator structure size to energy gained, it warrants obvious attention. RF frequency also impacts structure size as each cavity is nominally a half wavelength in diameter to within a Bessel root and pi, and the breakdown limits and gradients do improve with higher frequency. Working at the highest gradient possible and at the highest frequency should result in the most compact RF accelerating structures for a given design.

However, the size of an RF accelerating structure only dominates the size of an overall accelerator provided the majority of the machine is comprised of accelerating structures. For very high energy machines like the International Linear Collider (ILC), obtaining the highest gradient possible appreciably helps improve the cost and size of the linac, since at 500 GeV per linac system, there is ~15 km of linac to build. At much more modest energies (<500 MeV), the gradient and structure size have increasingly less impact on the overall machine design as the amount of space that is needed for ancillary beamline components like magnets, vacuum pumping, and diagnostics, as well as any low and high energy beam transport lines, diminishes the gains achieved in reducing active accelerating length. An example of a lower energy accelerator configuration and how these drifts relate to active acceleration in the accelerator structures (tanks) is shown in Fig. 7. For a given accelerator design, an expression can

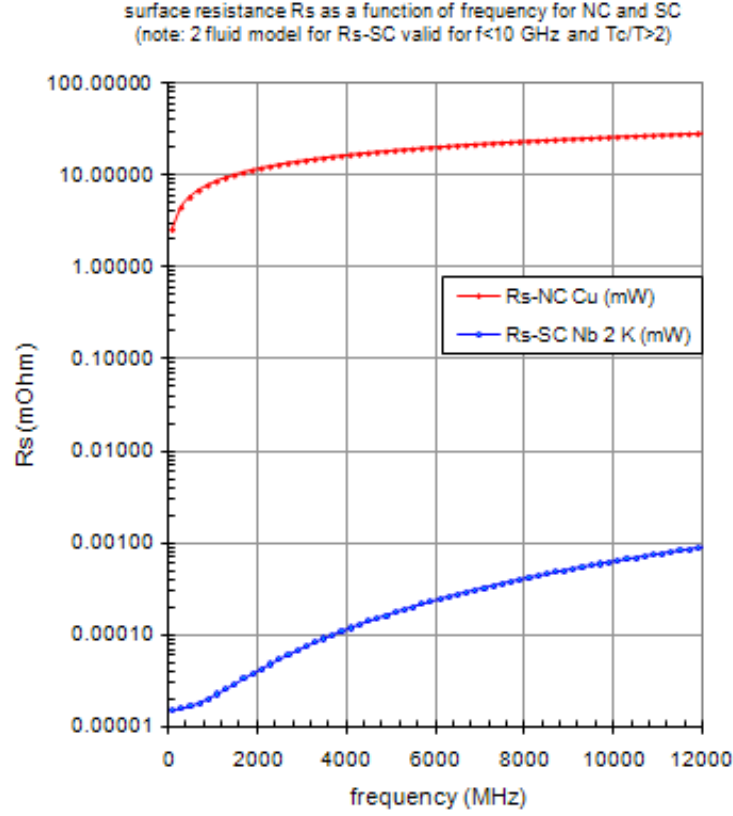


Figure 6: Plot of the surface resistance for normal conducting copper (red) and superconducting niobium (blue) at 2 K. The factor of ~ 30 increase in R_s from 1,500 to 12,000 MHz is the reason most SRF cavities are built to operate below $\sim 3,000$ MHz.

be developed to quantify the reduced impact of gradient and frequency on overall machine length:

$$L_{accel} = \left(\frac{T_0}{E_a} \right) \left(\frac{A_{tot}}{A_{tot} + D_{tot}} \right) = \left(\frac{T_0}{E_a} \right) f \quad (12)$$

where T_0 is the final energy out of the accelerator, E_a is the acceleration gradient in the structure, A_{tot} is the total active accelerating length, D_{tot} is the total length of beam drift distance, and f is the filling fraction of active to total length of the linac. Fig. 8 is a plot of how the filling factor scales with overall machine energy for a variety of structure gradients. For total machine energies below about 500 MeV, the active acceleration length can be 50% or less than the overall accelerator length, due to the fixed length of ancillary beamline drifts.

The importance of this decrease in filling fraction is shown in Fig. 9. As a function of total energy, the total lengths of machines are shown for different gradients. Because of the decrease in the filling factor at lower energy, and thus the importance of the accelerating structure in being able to influence the overall linac length, the percentage that length decreases due to doubling the gradient from 50 to 100 MV/m is less than 30% at 500 MeV. This highlights the importance of focusing attention on all aspects of machine design that contribute

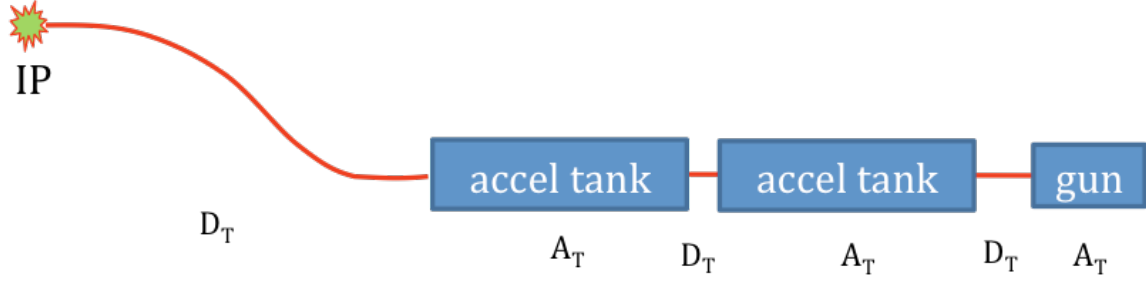


Figure 7: Conceptual design of a ~200-300 MeV linac showing how the active accelerating lengths in the structures (tanks) relate to ancillary drift lengths. The evaluations done include a nominal 8.5 m chicane to eliminate dark current bremsstrahlung at the IP.

to linac length. In the case presented, the high-energy dog leg needed to eliminate dark current at the interaction point adds appreciable length that erodes compactness. This suggests that research on reducing or eliminating dark current production and acceleration in both RF guns and high gradient acceleration structures would be an alternative way of achieving more compact accelerators for Compton backscatter systems.

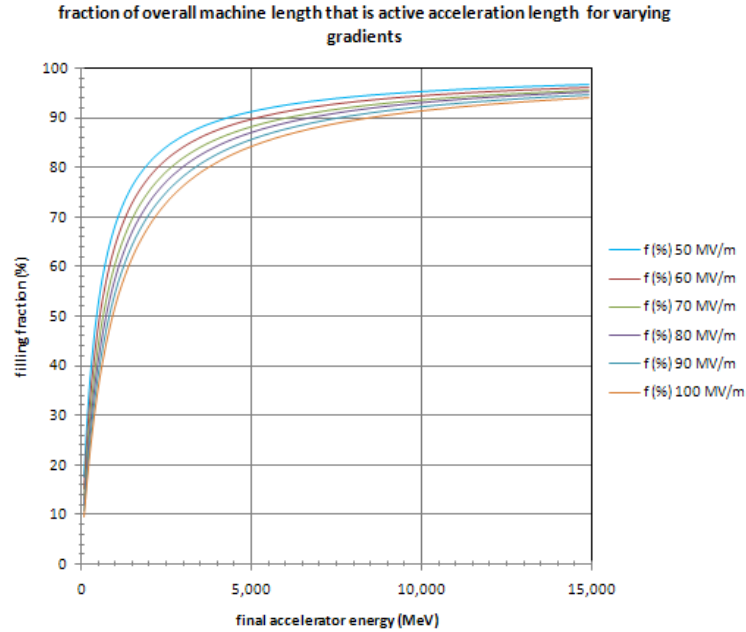


Figure 8: Plot showing how the percentage of active accelerating length varies as a function of overall accelerator output energy. For lower energy machines less than nominally 500 MeV (dashed green line), the amount of active accelerating length can be half or less of the overall machine length.

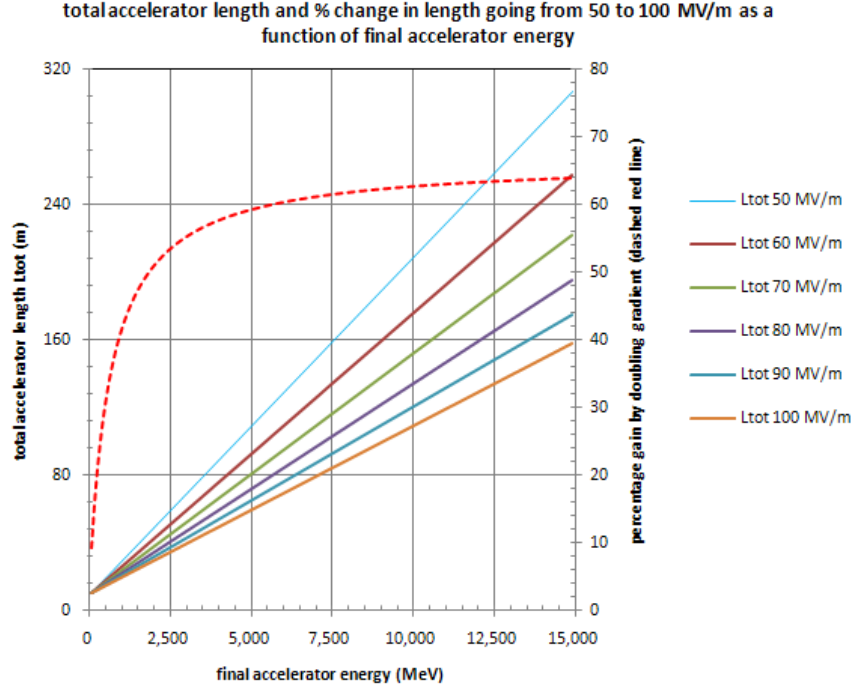


Figure 9: Plot of the total accelerator length for varying gradients as a function of overall machine energy, and the percentage change that length is reduced (red dashed line related to the right axis) as a function of final energy. Note that for machines with a nominal 8.5 m high energy drift section, the length of a 500 MeV (dashed green line) machine is only decreased around 30% if the structure

1.6 Conclusions

The accelerator technology available to produce electron beams suitable for Compton backscatter gamma ray sources is broad, and choosing the optimum approach is complicated. Adding in requirements for compactness or high average power further constrain the process. In this study, published data from references (papers and texts) were used to determine some of the tradeoffs possible to navigate the constrained design space.

While trends and generalities were highlighted regarding RF accelerator performance parameters important to compact Compton sources, it is important to note that for a much more accurate comparison and assessment, at least two relatively mature designs at two different frequencies should be evaluated side by side.

In general, application requirements need to be rigorously established spanning beam quality, compactness, mechanical ruggedness, and overall system robustness. These requirements then need to be weighed against the potential costs of a new “clean sheet” design built upon basic principles, compared to the cost savings from leveraging invested capability in a technology development area that comes “close enough” to meeting the requirements. Depending on the stringency of the requirements, there is always a compromise between cost savings and performance. Creating any accelerator system for deployable use in the field is a performance

application that requires there be ample engineering margin in the design to still allow for operation even under less than ideal circumstances.

2 Frequency Scaling in Beam Dynamics

In modern high-brightness RF linacs, the electron source is typically a photo-cathode RF gun, in which the cathode is integrated into the back-plane of the first cavity of a standing-wave RF structure. To first approximation, the laser pulse spatial and temporal dimensions determine the corresponding dimensions of the emitted electron bunch, allowing precise control of the initial electron beam parameters.

The key advantage of photo-cathode sources is that the emitted current density — and therefore, the peak brightness — can be made much higher than is possible with thermionic cathodes. As a result, the dynamics of dense beams produced in photo-guns is dominated by the repulsive self fields of the electron bunch. The design of photoinjector systems requires careful balancing of the space-charge forces with the accelerating and focusing forces provided by the RF fields and external magnetic optics.

Since the peak electric field one can achieve in a given RF structure depends on frequency, the balance of space-charge and accelerating forces places limits on the beam parameters that can be chosen. From the γ -ray source point of view, we need to maximize Eq. 4 as a function of number of electrons per bunch and RF frequency.

The optimization of an RF photoinjector design usually requires a search of a large parameter space, which includes RF field amplitudes, initial beam size, duration and charge, focusing lens position and strength, and gun-to-linac separation. This involved process must include RF and magnet design calculations and multi-particle simulations. It is very convenient therefore, to begin a design by scaling either charge or RF frequency (or both) from a previously optimized design using the relevant transverse and longitudinal dynamics equations. We proceed here by reviewing these equations and discussing the implications of frequency scaling.

2.1 Longitudinal Motion

In the case of longitudinal motion, we can begin by reviewing the single particle equations of motion, as collective effects are to some degree less important here than in the transverse case. The RF accelerating field in a π -mode standing wave accelerator can be modeled as a sinusoidal field in longitudinal position and time (ignoring spatial higher harmonics) and, as shown by Kim [8], leads to an energy gain given by

$$\frac{d\gamma}{dz} = \frac{eE_p}{2m_e c^2} [\sin(\phi) + \sin(\phi + 2k_{RF}z)], \quad (13)$$

where $k_{RF} = \omega/c$ is the RF wave number, E_p is the peak accelerating field, and $\phi = k_{RF}z - \omega t + \phi_0$ is the phase relative to the forward traveling component of the standing wave. The phase convention here has maximum acceleration when $\phi = \pi/2$. This phase depends in turn on the particle velocity and changes according to

$$\frac{d\phi}{dz} = k_{RF} \left[1 - \frac{\gamma}{\sqrt{\gamma^2 - 1}} \right]. \quad (14)$$

Table 1: Accelerating field strengths used in $E_p \propto f^{1/2}$ scaling study

RF Frequency (GHz)	E_p (MV/m)	α
1.428	84.9	2.77
2.856	120	1.96
5.712	169.7	1.39
11.424	240	0.98
22.848	339.4	0.69

These equations can be generalized to any frequency by substituting $\zeta = k_{RF}z$, giving

$$\frac{d\gamma}{d\zeta} = \alpha [\sin(\phi) + \sin(\phi + 2\zeta)] \quad (15)$$

$$\frac{d\phi}{d\zeta} = 1 - \frac{\gamma}{\sqrt{\gamma^2 - 1}} \quad (16)$$

where $\alpha = eE_0/2k_{RF}m_e c^2$ parameterizes the particle motion in the applied RF field. This parameter is the normalized RF vector potential, and can be thought of as the average energy gain (in units of $m_e c^2$) per RF radian. The immediate frequency scaling result here is that one can maintain exactly the longitudinal dynamics by making α constant, or $E_p \propto f$.

$E_p \propto f$ scaling of beam dynamics has been studied by Rosenzweig and Colby [9], and their methods and results will be discussed further below. It is useful at this point however, to consider Eqns. 15 and 16 more carefully in cases where α is not constant. As we have seen above, in practice, linear scaling of peak field with frequency is too optimistic and a variety of different scalings have been proposed. We choose to analyze the original Kilpatrick scaling, $E_p \propto f^{1/2}$, as it represents an average of the different studies discussed above and models reasonably well the results of different operational photoinjectors [10, 11]. The specific values of peak acceleration fields and α ($\propto f^{-1/2}$) considered in this study are based on achieved fields at S- and X-band, and are given in Table 1.

Given initial conditions at the photocathode ($\gamma_0 \approx 1$ and $\phi = \phi_0$), Eqns. 15 and 16 can be numerically integrated to find the particle dynamics. With an appropriate choice of ϕ_0 , particles initially gain energy at a rate $d\gamma/dz \approx 2\alpha k_{RF} \sin(\phi_0)$ and slip significantly in phase while the particle is nonrelativistic. As energy increases, the phase slippage is arrested and an asymptotic value is reached. An approximate expression for this asymptote is found by Kim [8],

$$\phi_\infty = \frac{1}{2\alpha \sin \phi_0} + \phi_0. \quad (17)$$

As one might expect, the amount of phase slippage increases as α decreases. At low enough values of α , particles are not ‘captured’ by the forward wave component of the RF fields and there is no net acceleration (averaged over an RF cycle). In fact there is a tighter restriction on α (and therefore field strength) than a simple capture criterion. Kim’s analysis finds that a transverse emittance is induced due to the phase dependence of the radial force applied by the RF fields. This *RF emittance*, ε_{RF} , is minimized when the structure exit phase is $\pi/2$, and away from the minimum increases as $\varepsilon_{RF} \propto |\cos \langle \phi \rangle|$.

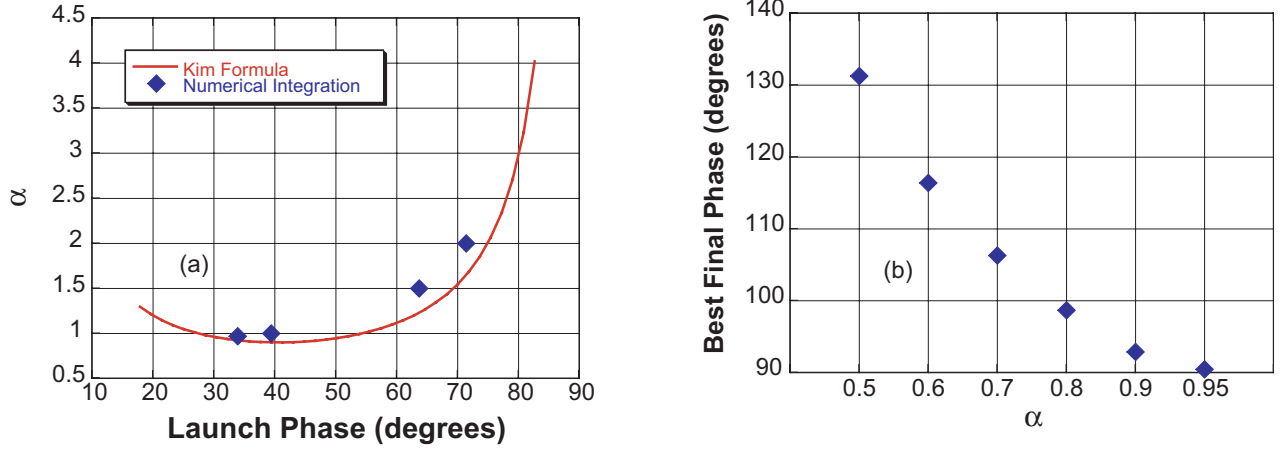


Figure 10: (a) Plot of electron launch phase required to produce an asymptotic phase for best emittance ($\phi_\infty = \pi/2$) versus α . Here 90 degrees corresponds to the peak accelerating field and lower launch phases indicate injection as the cathode field is increasing in time. For $\alpha \lesssim 0.96$ particles slip past $\pi/2$ regardless of injection phase. In (b) the least possible slippage past $\phi_\infty = \pi/2$ is plotted versus α .

An optimized design must therefore produce $\phi_\infty = \pi/2$. Substitution in Eq. 17 shows the condition the initial launch phase should meet,

$$\alpha = \frac{1}{(\pi - 2\phi_0) \sin \phi_0}. \quad (18)$$

This formula is plotted in Fig. 10 along with some values of launch phase required to produce $\phi_\infty = \pi/2$ calculated by numerical integration of Eqns. 15 and 16. As the plot shows, for $\alpha \lesssim 0.96$ (as determined by the numerical integrations), the amount of phase slippage is too great to capture with optimal exit phase, regardless of launch phase. Part (b) of the plot shows that as α continues to decrease, the asymptotic phase slips farther behind the peak accelerating field.

Before proceeding to consider transverse motion, there are a few conclusions we can draw about the implications of $\alpha \propto f^{-1/2}$ scaling. Firstly, there is a high frequency cut-off above which α is too small for a photoinjector to operate effectively. This cut-off occurs when $\alpha \approx 1$ (at roughly 11 GHz assuming the fields given in Table 1). This restriction applies strictly to the photoinjector, where particles must be accelerated from rest to relativistic energies in a small fraction of an RF cycle. Post-injector structures may operate perfectly well with low α and thus, higher frequencies.

In the injector, phase slippage past 90 degrees has a number of deleterious effects: (1) The RF-induced emittance will be significantly larger than the minimum described in the scaling rules below. (2) When injecting below 90 degrees, the dependence of phase slippage on ϕ_0 tends to compress the bunch (see Eq. 17). In high current beams longitudinal space-charge counters this effect resulting in minimal change in bunch length from the cathode. In cases where the bunch slips behind crest however, these effect add and significant bunch lengthening can occur. This bunch lengthening compounds the growth in RF emittance as well as

increases the energy spread of the beam. (3) The need to use low injection phases in low- α systems makes them more sensitive to jitter in RF phase and power. Because the Schottky effect changes the quantum efficiency of the cathode with applied electric field, a lower launch phase makes a set amount of RF phase jitter cause a relatively larger fluctuation in emitted charge. This in turn will lead to an increased shot-to-shot fluctuation in emittance, energy spread, and beam pointing through wakefields and misaligned elements.

2.2 Scaling and Transverse Motion

In cases where $\alpha \gtrsim 1$ is achievable, we seek to determine how the average transverse brightness, $\mathcal{B} = N_e f_{rep} / \varepsilon_n^2$, our Compton source figure of merit, or for a single bunch, Q / ε_n^2 , scales with RF frequency. To do this, we must consider the transverse beam dynamics. It is instructive to follow the analysis of Ref. [9], in which this scaling was investigated in the case of constant α ($E_p \propto f$ scaling).

As mentioned above, Eqns. 15 and 16 lead to exact scaling of longitudinal motion in the normalized variable, ζ , if α is constant. Thus, given a proven RF structure design, linear scaling of all dimensions results in constant particle output energy. In considering an electron bunch as opposed to single particles, it is clear that the RMS bunch length, σ_z , must scale with λ_{RF} in order to maintain a constant bunch length as measured in RF degrees, σ_ϕ . Constant σ_ϕ ensures that the RF curvature induced energy spread, which scales as σ_ϕ^2 , is kept constant. Because the Compton source performance is very sensitive to energy spread, we must enforce the scaling

$$\sigma_z \propto \lambda_{RF} \quad (19)$$

regardless of the chosen field strength scaling. Given this bunch length scaling and constant injector exit energy ($\gamma_{inj} = \text{constant}$), we can ensure that undesired bunch lengthening effects due to longitudinal space-charge forces are not present by preserving the peak beam current, $I = \text{constant}$, and therefore,

$$Q \propto \lambda_{RF}. \quad (20)$$

The scaling of the transverse beam dynamics can be deduced by examining the RMS transverse envelope equation. For the purposes of this study, we consider the envelope equation describing the evolution of a cylindrically symmetric beam in the absence of thermal emittance effects [12],

$$\sigma_r'' + \frac{\gamma'}{\gamma} \sigma_r' + k_\beta^2 \sigma_r = \frac{I}{\gamma^3 I_0 \sigma_r}, \quad (21)$$

where primes indicate differentiation with respect to z , k_β is the focusing wave number due to externally applied RF and magnetic fields, and $I_0 = 17\text{kA}$, is the electron characteristic current. The thermal emittance term, as well those due to RF curvature and chromatic aberration in magnetic optics are not included in Eq. 21 since they are typically much smaller than the space-charge term. Once the the scaling required to satisfy the balance of space-charge and RF forces is determined however, the scaling of these other emittance terms will be readily found.

The transverse dynamics are scaled by equal scaling of the space-charge defocusing (imaginary) wave number, given by

$$\kappa_{SC}^2 = \frac{I}{\gamma^3 I_0 \sigma_r^2} = \frac{c}{\gamma^3 I_0} \cdot \left(\frac{Q}{\sigma_z \sigma_r^2} \right), \quad (22)$$

with the external focusing wave number, k_β^2 . For RF focusing, we have [13]

$$k_\beta^2 \propto \frac{F_{RF}}{r} = \frac{e}{2} \frac{dE_z}{dz} \propto \frac{E_p}{\lambda_{RF}}. \quad (23)$$

At this point we are free to choose the scaling of E_p . In $E_p \propto f$ scaling, as studied in Ref. [9], k_β^2 scales as λ_{RF}^{-2} . Given the condition, $Q/\sigma_z = \text{constant}$, set by longitudinal considerations, we would require $\sigma_r \propto \lambda_{RF}$ for κ_{SC} to scale properly. Thus, in this scaling, all beam dimensions and focal lengths scale linearly with λ_{RF} . In fact, in Ref. [9] simulations are performed using these scaling rules and agreement between simulations and theory are found to be excellent.

Since we wish to consider the more realistic scaling, $E_p \propto f^{1/2}$, we see from Eq. 23 that

$$k_\beta^2 \propto \frac{1}{\lambda_{RF}^{3/2}}, \quad (24)$$

and therefore, the transverse spot size must scale as

$$\sigma_r \propto \lambda_{RF}^{3/4}. \quad (25)$$

The scaling of emittance is found by summing in quadrature the contributions of different emittance sources. The most significant terms are space-charge, thermal, RF, and chromatic aberration induced,

$$\varepsilon_{tot}^2 = \varepsilon_{SC}^2 + \varepsilon_{th}^2 + \varepsilon_{RF}^2 + \varepsilon_{\Delta p}^2. \quad (26)$$

The space-charge induced residual emittance is given by [14]

$$\varepsilon_{SC} \propto k_\beta \sigma_r^2 \propto \lambda_{RF}^{3/4}. \quad (27)$$

The thermal emittance is simply proportional to the beam size emitted from the cathode,

$$\varepsilon_{th} \propto \sigma_r \propto \lambda_{RF}^{3/4}. \quad (28)$$

The RF induced emittance [8] (when $\phi_\infty = \pi/2$) scales as

$$\varepsilon_{RF} \approx \left(\frac{eE_p}{\sqrt{8}m_e c^2} \right) (k_{RF} \sigma_z)^2 \sigma_r^2 \propto \frac{1}{\lambda_{RF}^{1/2}} \cdot 1 \cdot \lambda_{RF}^{3/2} \propto \lambda_{RF}. \quad (29)$$

Finally, the emittance contribution from chromatic aberrations in magnetic optics is given by

$$\varepsilon_{\Delta p} \propto \left(\frac{\Delta p}{p} \right) \left(\frac{\sigma_r^2}{f} \right) \propto (k_{RF} \sigma_z)^2 k_\beta \sigma_r^2 \propto \lambda_{RF}^{3/4}. \quad (30)$$

The total emittance therefore, scales as

$$\varepsilon_{tot}^2 \propto a \lambda_{RF}^{3/2} + b \lambda_{RF}^2, \quad (31)$$

where a and b are undetermined constants. The Compton source figure of merit therefore, scales as

$$\mathcal{B} = \frac{Q}{\varepsilon^2} \propto \frac{\lambda_{RF}}{a \lambda_{RF}^{3/2} + b \lambda_{RF}^2}. \quad (32)$$

At long enough wavelengths, we see that the RF term must dominate the total emittance and we get $\mathcal{B} \propto \lambda_{RF}^{-1}$. As the RF wavelength decreases, the other emittance terms dominate and $\mathcal{B} \propto \lambda_{RF}^{-1/2}$. In either case, the brightness increases with RF frequency, and we must conclude that it is advantageous to scale the photoinjector to the highest frequency that maintains the condition $\alpha \gtrsim 1$, or roughly 11 GHz.

2.3 Scaling Simulations

In this section, multi-particle simulations are presented, the purpose of which are to test the scaling rules hypothesized above. We use the code, PARMELA [15], which is a time domain program that allows the import of externally generated RF and magnetic field profiles and computes space-charge forces in the ‘quasi-static’ approximation, where Coulomb forces are computed in the rest frame of the average beam particle and transformed and applied in the lab frame.

To set up the scaling simulations, we must address two subtle points of $E_p \propto f^{1/2}$ scaling that have not been discussed above. First, we have assumed above that the injector output energy is independent of frequency. This was shown to be the case with $E_p \propto f$ scaling. With decreasing α however, the energy gain per cell decreases, and the structure must use more cells. We adopt the rule

$$N_{\text{cell}} \propto \alpha^{-1/2} \propto f^{1/2}, \quad (33)$$

in order to maintain an injector output energy, and therefore longitudinal dynamics, independent of frequency. The actual number of cells must of course, be $n + 1/2$, where n is an integer, so that 1.5 cell structures were used in the 1.4 and 2.8 GHz simulations, increasing to 4.5 cells in the 23 GHz simulation.

The second subtle issue is that of bunch lengthening due to image charge effects at the photo-cathode. The image charge induced longitudinal electric field at the cathode is counter to the accelerating RF field and scales as

$$E_{SC} \propto \frac{Q}{\sigma_r^2} \propto \lambda_{RF}^{-1/2} \propto E_p. \quad (34)$$

This effect is therefore transparent to frequency scaling, provided that the launch phase is the same in all cases. As we have already seen, this is a problematic assumption. The amount of phase slippage in the photo-gun depends on α , and the longitudinal dynamics of $E_p \propto f^{1/2}$ scaling favor lower launch phases at higher frequencies. As α approaches one, we find that the coupling between transverse and longitudinal dynamics implied by Eq. 34 tends to break down the brightness scaling law given by Eq. 32, thus re-emphasizing the importance of the criterion $\alpha \gtrsim 1$.

The T-REX (Thomson-Radiated Extreme X-rays) photoinjector [11] is used as the baseline design which is frequency scaled in the PARMELA simulations shown below. This design uses a 1.6 cell, S-band photo-gun and SLAC-type traveling wave accelerator sections to produce the electron beam. The parameters of the design are loosely based on the so-called LCLS ‘working point,’ [16] and are summarized in Table 2. This is a well-optimized design that uses the emittance compensation technique [17] to control the potential growth of emittance due to strong space-charge forces in the 100 Amp peak current electron bunch. The evolution of the beam spot size and emittance as it is accelerated through the system is shown in Fig. 11. The final simulated emittance of 0.6 mm mrad (rms, normalized) is an excellent result for 1 nC of beam charge and would be very well suited to drive Compton-scattering light sources.

The PARMELA simulations were carried out by scaling the beam and accelerator parameters with frequency as indicated in Table 2. In each case, the focusing solenoid strength and launch phase at the photo-cathode were fine tuned to minimize the emittance. As predicted above, it was in fact found that the best emittance occurred at lower launch phases in the higher

Table 2: S-band parameter set used as the baseline for frequency scaling simulations.

Parameter	Value	Scaling
Cathode field	120 MV/m	$f^{1/2}$
Drift distance to section	150 cm	$f^{-3/4}$
Charge	1 nC	f^{-1}
Temporal Profile	10 psec flat-top	f^{-1}
Spatial Profile	Clipped gaussian, $\sigma_r = 1.0$ mm, $r_{cut} = 0.85$ mm	$f^{-3/4}$

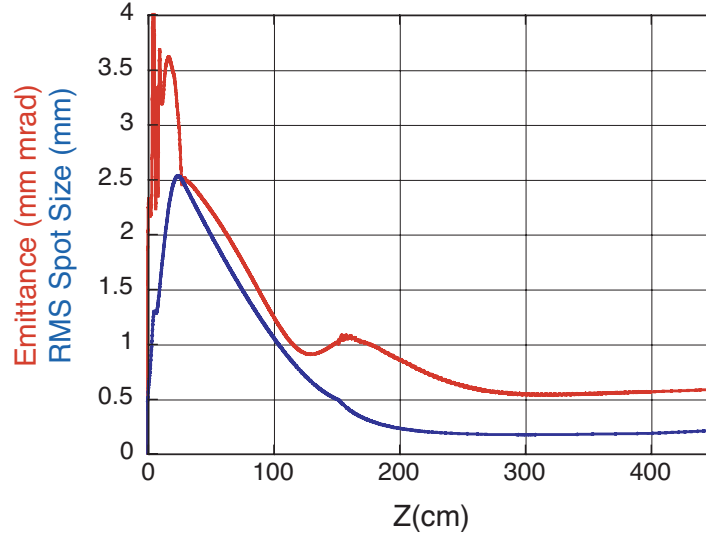


Figure 11: Evolution of the emittance and beam size in the optimized baseline design. The baseline frequency is 2.856 GHz.

frequency simulations. The optimal launch phase varied from 37 degrees at L-band to 20 degrees at X-band and 15 degrees at K-band.

At this point the transverse beam size on the cathode was allowed to deviate from strict $f^{-3/4}$ scaling to observe the emittance variation. We found lower emittances by increasing the cathode spot size in the high frequency simulations and decreasing the spot size in the L-band simulation. Given the required variation in launch phase (and therefore effective reduction of $E_{cathode}$ at higher frequencies) this result is consistent with the image charge induced bunch lengthening effect described by Eq. 34 above. The emittance is plotted versus longitudinal position (divided by the scaled focusing wavenumber, $k_\beta \propto f^{3/4}$) for the lowest 4 frequencies in Fig. 12. Final emittance and brightness (Q/ε^2) are plotted versus frequency in Fig. 13.

As Fig. 13 shows, the simulated emittance scaling is $\varepsilon \propto f^{-0.7}$. This indicates that, even at 1.4 GHz, the RF emittance term is negligible. The observed slightly weaker scaling than predicted by the other term in Eq. 31 ($\varepsilon \propto \lambda_{RF}^{3/4}$) is consistent with our deviation from strict scaling of the cathode spot size. Also apparent from Fig. 13 is that the scaling rules break down completely in the 22.8 GHz simulation. Here the low value of α causes significant emittance growth due both to bunch lengthening and RF effects from phase slippage in the first cells ($\phi_\infty > \pi/2$). Figure 14 gives evidence of this problem by plotting the accelerating field seen by

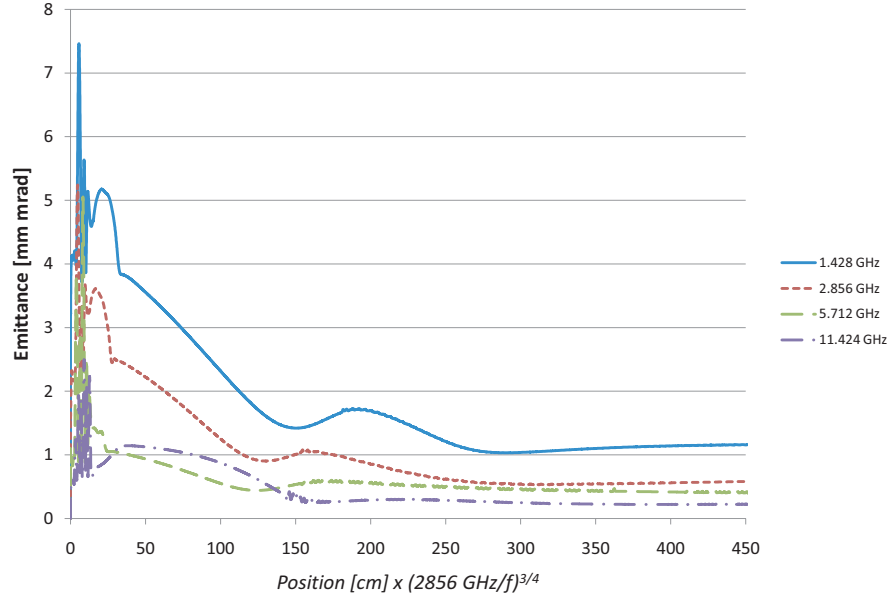


Figure 12: PARMELA simulations of the emittance dynamics in the L-, S-, C-, and X-band systems. Note that while the final emittance in the X-band simulation is lowest, the shape of the curve deviates significantly from that of the others, indicating the beginning of scaling breakdown.

the electrons in the RF gun. The field goes negative before exiting each cell, indicating a phase greater than $\pi/2$.

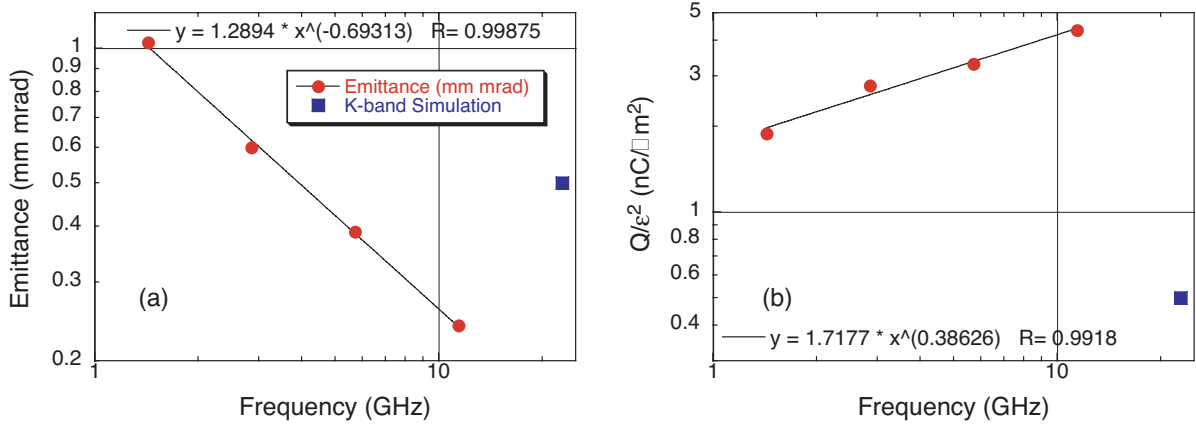


Figure 13: Simulated (a) emittance and (b) brightness plotted log-log versus RF frequency. Power law fits show a predictable, but slightly weaker scaling than predicted by Eqns. 31 and 32 up to X-band. The scaling laws break down at higher frequency and the beam quality decreases.

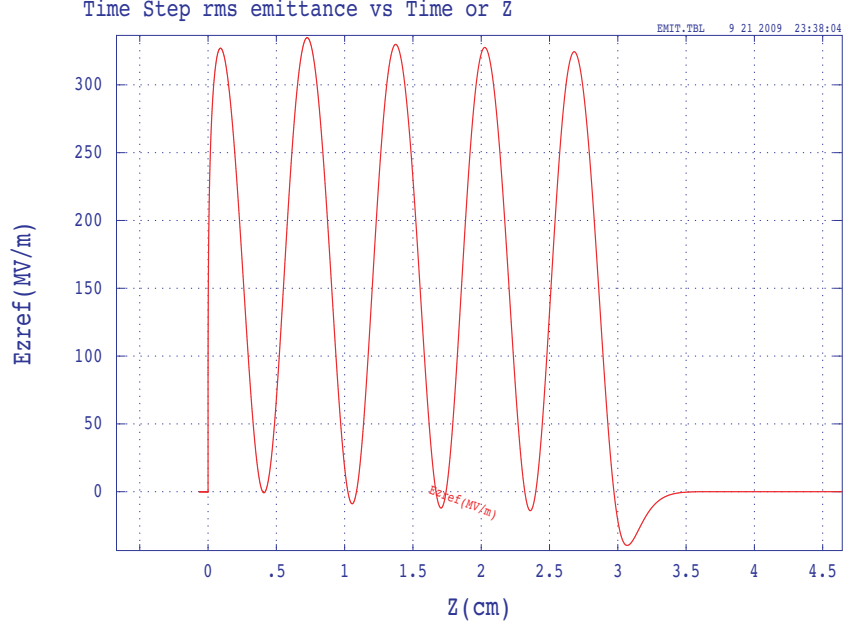


Figure 14: Longitudinal component of the RF electric field applied to the beam in the simulation at 22.8 GHz. Negative values near the cell irises indicate too much phase slippage and result in RF emittance growth.

2.4 Conclusions of Beam Dynamics

Analytical scaling of injector design with frequency is robust only when one assumes $E_p \propto f$ can be achieved. If this is not feasible, as indicated by experimental data, the scaling of transverse dynamics cannot be strictly followed as adjustments must be made to compensate for differences in longitudinal dynamics (varying α). Above the frequency at which α drops below 1, longitudinal dynamics make photo-guns unattractive.

The simulation study performed here assumed $E_p \propto f^{1/2}$ scaling and $E_p = 120$ MV/m at S-band. This study found a moderate increase in average beam brightness with frequency ($Q/\varepsilon^2 \propto f^{0.4}$) up to roughly 11 GHz, beyond which we observe emittance increase and brightness decrease driven by the longitudinal effects discussed above.

3 Interaction Laser

In designing the optimal Compton-scattering source for any particular application, it is important to consider the laser technology. In addition to the direct impact on the gamma rays, the laser and electron pulses must match, so the available laser technology can inform the selection of the linac architecture. There is, by the nature of the source, at least one laser required: the “interaction laser”. This is the laser that provides the photons which actually scatter from the electron bunch. Depending on the electron beam technology used there might be one or more additional lasers. For example, if laser wakefield acceleration is being used, there will be a large, high-intensity laser system driving the electrons. If an rf photoinjector and rf linac are

used, then a well-shaped laser is needed to generate the electrons at the cathode.

In this study, we will focus on the interaction laser, something common to all architectures. The ideal parameters for this laser will be found, followed by an overview of the current state of the art in that particular parameter space and a discussion of where future developments can take us.

3.1 Optimal Parameters

Optimizing the interaction laser for a Compton source depends on the details of the final application. The most significant question: is a narrow bandwidth, short pulse, or high flux required? The short-pulse case requires either compressing the electron bunch (degrading the beam emittance) or using an ultrafast laser (with necessarily larger bandwidth), either of which will lead to an increase in the gamma ray bandwidth. Much of the advantage of a Compton source comes from its monochromaticity, however, and most applications don't need fs-scale resolution, so here we choose to focus on the "narrow bandwidth" case.

In order to scatter the maximum number of laser photons in a Compton-scattering source, each electron needs to see as many photons as possible as it travels through the laser pulse. Stated mathematically, for each electron

$$N_s = \int n_l(x, y, z, t) \sigma_s dl$$

where N_s is the number of photons scattered, n_l is the density of the photons, σ_s is the scattering cross-section ($6.652 \times 10^{-25} \text{ cm}^2$ for Thomson scattering), and the integral is performed along the path of the electron's travel. This integral is a column density, which is what needs to be maximized to optimize the total scattered photon flux. This can be done by increasing either the total photon density n_l or the length of travel of an electron through a given n_l .

Nonlinear effects limit the peak laser intensity an electron can see without degrading the bandwidth of the scattered photon spectrum. For example, if the electron's transverse motion starts to become relativistic, the effective forward velocity of the electron is reduced, lowering the scattered photon energy. In the Thomson scattering limit, the energy of a scattered photon, including this effect, is given by

$$\omega_{obs} = \omega_{inc} \frac{2\gamma^2 (1 + \beta \cos \theta_{inc})}{1 + \frac{a_0^2}{2} + \gamma^2 \theta_{obs}^2}$$

which is a standard result from synchrotron physics (see [18], Ch. 5), where the undulator parameter K which measures the magnetic field strength is replaced with the laser parameter $a_0 = \frac{eE_0}{mc\omega} \propto \sqrt{n_l}$ which measures the electric field strength. Thus, as the scattering electron sees a variation of a_0 while transiting the laser pulse, the scattered photons will have a range of energies as well. This effect puts a cap on how far n_l can be increased.

Limiting the peak value of a_0 to a specific value, the laser pulse length can then be increased to maximize the electron path integral above. However, the density of both photons and electrons falls as you move longitudinally away from the interaction point due to diffraction effects of the laser and the beam envelope evolution of the electrons. There is thus an upper limit on how long the pulse can grow while still contributing to the gamma ray flux. To

optimize the overall efficiency of photon scattering, it's also worth minimizing the total energy required to reach that a_0 value, so minimizing the focal spot size and pulse length also have advantages.

In summary, to maximize the scattered photon flux, you want to:

1. Maximize the laser photon density subject to the nonlinear limit.
2. Maximize the laser pulse length.
3. Minimize the laser energy needed to reach that limit by:
 - (a) Minimize the interaction spot size based on electron beam properties [correlated and uncorrelated angular distributions (emittance)] This increases the electron density and reduces the total number of photons needed to reach the desired photon density.
 - (b) Limit length maximization based on diminishing return due to beam expansion effects.

3.1.1 Laser Propagation Preliminaries

First, let's define some parameters to describe the laser field. Gaussian laser propagation is described by the normalized field intensity[19]

$$\tilde{u}(x, y, z) = \left(\frac{2}{\pi}\right)^{1/2} \frac{\exp[-ikz + i\psi(z)]}{w(z)} \exp\left[-\frac{x^2 + y^2}{w^2(z)} - ik\frac{x^2 + y^2}{2R(z)}\right] \quad (17.1)$$

where $w(z) = w_0\sqrt{1 + \frac{z^2}{z_r^2}}$ is the laser $1/e^2$ intensity radius, w_0 is the focused laser spot size, $z_r = \frac{\pi w_0^2}{\lambda}$ is the laser rayleigh range, and $R(z)$ is the wavefront radius of curvature. Scaling to a peak field of E_0 , adding in the temporal oscillation and gaussian pulse length, and including the polarization produces the electric field

$$\mathbf{E}(x, y, z, t) = \frac{E_0 w_0}{w(z)} e^{-i[kz - \omega t - \psi(z)]} \exp\left[-\frac{x^2 + y^2}{w^2(z)} - \frac{(kz - \omega t)^2}{(\omega\tau)^2}\right] \exp\left[-ik\frac{x^2 + y^2}{2R(z)}\right] \hat{x}$$

(where any focusing effect on the polarization vector of the light are neglected - a condition similar to that of the paraxial approximation used to get the equation in the first place) and the commensurate magnetic field

$$\mathbf{H}(x, y, z, t) = \frac{E_0 w_0}{c\mu_0 w(z)} e^{-i[kz - \omega t - \psi(z)]} \exp\left[-\frac{x^2 + y^2}{w^2(z)} - \frac{(kz - \omega t)^2}{(\omega\tau)^2}\right] \exp\left[-ik\frac{x^2 + y^2}{2R(z)}\right] \hat{y}.$$

We can use these two fields to find the power flow through a given point with

$$\mathbf{S}(x, y, z, t) = \frac{1}{2} \mathbf{E} \times \mathbf{H}^* = \frac{E_0^2 w_0^2}{2c\mu_0 w^2(z)} \exp\left[-\frac{2(x^2 + y^2)}{w^2(z)} - \frac{2(kz - \omega t)^2}{(\omega\tau)^2}\right] \hat{z} \propto n_l \hat{z}.$$

We can convert this field into a measurement of the total energy by integrating the power crossing the $z = 0$ plane at all time:

$$\begin{aligned} E(E_0, w_0, \tau) &= \int_{-\infty}^{\infty} \int_{-\infty}^{\infty} \int_{-\infty}^{\infty} \mathbf{S}(x, y, 0, t) \cdot \hat{z} \, dx \, dy \, dt \\ &= \frac{E_0^2 w_0^2 \tau}{2c\mu_0} \left(\frac{\pi}{2} \right)^{\frac{3}{2}} \end{aligned}$$

3.1.2 Bandwidth Effects

We begin our analysis by looking at the on-axis γ -ray bandwidth ($\theta_{inc} = \theta_{obs} = 0$), where

$$\omega_x = \frac{4\gamma^2 \omega_{inc}}{1 + a_0^2/2}$$

We will normalize the x-ray energy by $4\gamma^2 \omega_{inc}$ for the remainder of this section. The observed spectrum from a single electron can be determined by scaling the normalized spectrum produced at each moment in time by number of photons scattered at that time. We assume we are in the Thomson scattering limit and neglect any recoil of the electron (which can only further broaden the spectrum). We further assume an electron moving uniformly along the z axis with a velocity $-v\hat{z}$ crossing $z = 0$ at $t = 0$, which means $x_e(t) = y_e(t) = 0$, $z_e(t) = -vt \approx -ct$. Then we have

$$N(\omega_x) = \int_{-\infty}^{\infty} S(t) F(\omega_x, t) dt$$

where $S(t) = S(0, 0, -ct, t)$ is the Poynting vector magnitude (photon density) the electron sees for scattering at time t and $F(\omega, t)$ is the spectrum emitted at time t . The spectrum of a single scattering event off a single electron is given by

$$F(\omega_x, t) = \delta(\omega_x - \omega_x(t))$$

where

$$\omega_x(t) = \left(1 + \frac{a_0^2(t)}{2} \right)^{-1}$$

and

$$a_0^2(t) = \left(\frac{eE(0, 0, -ct, t)}{mc\omega} \right)^2 = \frac{a_0^2}{2} \frac{w_0^2}{w^2(ct)} e^{-\frac{8t^2}{\tau^2}}$$

with $a_0 = \frac{eE_0}{mc\omega}$, where we have used the time-averaged value of E . To perform the integral, we need to transform the delta function of ω to one of t , which can be done using [20]

$$\delta[g(t)] = \sum_{a, g(a)=0, g'(a) \neq 0} \frac{\delta(t-a)}{|g'(a)|}.$$

Since $g(t) = \omega_x - \omega_x(t)$, $a = t(\omega_x)$ where $t(\omega_x(t')) = t'$ or $t(x) = \omega_x^{-1}(x)$. Now we have

$$N(\omega_x) = \int_{-\infty}^{\infty} S(t) \frac{\delta[t - t(\omega_x)]}{\left| \frac{d}{dt} [\omega_x - \omega_x(t)] \right|_{t=t(\omega_x)}} dt = \frac{S[t(\omega_x)]}{\left| \frac{d}{dt} [-\omega_x(t)] \right|_{t=t(\omega_x)}}$$

Performing the differentiation:

$$-\frac{d}{dt} \left(1 + \frac{a_0^2(t)}{2} \right)^{-1} = \left(1 + \frac{a_0^2(t)}{2} \right)^{-2} \frac{1}{2} \frac{d}{dt} a_0^2(t) = \frac{1}{2} \omega_x^2(t) \frac{d}{dt} a_0^2(t)$$

and

$$\begin{aligned} \frac{d}{dt} a_0^2(t) &= \frac{d}{dt} \left(\frac{a_0^2}{2} \frac{w_0^2}{w_0^2(1 + \frac{c^2 t^2}{z_r^2})} e^{-\frac{8t^2}{\tau}} \right) \\ &= - \left(\frac{1}{1 + \frac{c^2 t^2}{z_r^2}} \frac{2c^2 t}{z_r^2} + \frac{16t}{\tau^2} \right) a_0^2(t) \end{aligned}$$

and so

$$\frac{d}{dt} [-\omega_x(t)] = -\frac{1}{2} \omega_x^2(t) \left(\frac{1}{1 + \frac{c^2 t^2}{z_r^2}} \frac{2c^2 t}{z_r^2} + \frac{16t}{\tau^2} \right) a_0^2(t)$$

and since

$$S(t) = \frac{m^2 c \omega^2}{\mu_0 e^2} a_0^2(t)$$

we find that

$$N(\omega_x) = \frac{m^2 c \omega^2}{\mu_0 e^2} \left| -\frac{1}{2} \omega_x^2(t) \left(\frac{1}{1 + \frac{c^2 t^2}{z_r^2}} \frac{2c^2 t}{z_r^2} + \frac{16t}{\tau^2} \right) \right|^{-1} \Big|_{t=t(\omega_x)}$$

Using the software *Mathematica* to find $t(\omega_x)$

$$t(\omega_x) = \frac{1}{2\sqrt{2}} \sqrt{\tau^2 W \left(\frac{a_0^2 \omega_x}{2(1 - \omega_x)} e^{\tau_0^2/\tau^2} \frac{\tau_0^2}{\tau^2} \right) - \tau_0^2}$$

where $\tau_0^2 = \frac{8\pi^2 w_0^4}{c^2 \lambda^2}$ and $W(z)$ is the Lambert W -function, the inverse of the function $f(z) = ze^z$. A plot of $N(\omega_x)$ is shown in Fig. 15, where we have assumed $\tau = 10$ ps, $w_0 = 20$ μ m, and $\lambda = 532$ nm (giving $z_r = 2.3$ mm). As can be seen, for even modest values of a_0^2 broadening of the on-axis spectrum can be seen. This implies we want to keep $a_0^2 < 0.001$ to maintain a narrow bandwidth.

3.1.3 Longitudinal Limits

Having determined an optimal photon density, the next step is to find the appropriate laser pulse length. To calculate the relative amount of scattering as a function of laser pulse length, we can perform the column integral for a single electron. Making the same assumptions as above (being in the Thomson scattering limit with an electron moving uniformly along the z axis), we find the total number of scattered photons N_s to be

$$N_s(E_0, w_0, \tau) \propto \int_{-\infty}^{\infty} \mathbf{S}(0, 0, -ct, t) \cdot \hat{\mathbf{z}} dt = \frac{E_0^2 \pi z_r}{2c^2 \mu_0} e^{\frac{8z_r^2}{c^2 \tau^2}} \left(1 - \operatorname{erf} \frac{2\sqrt{2} z_r}{c \tau} \right)$$

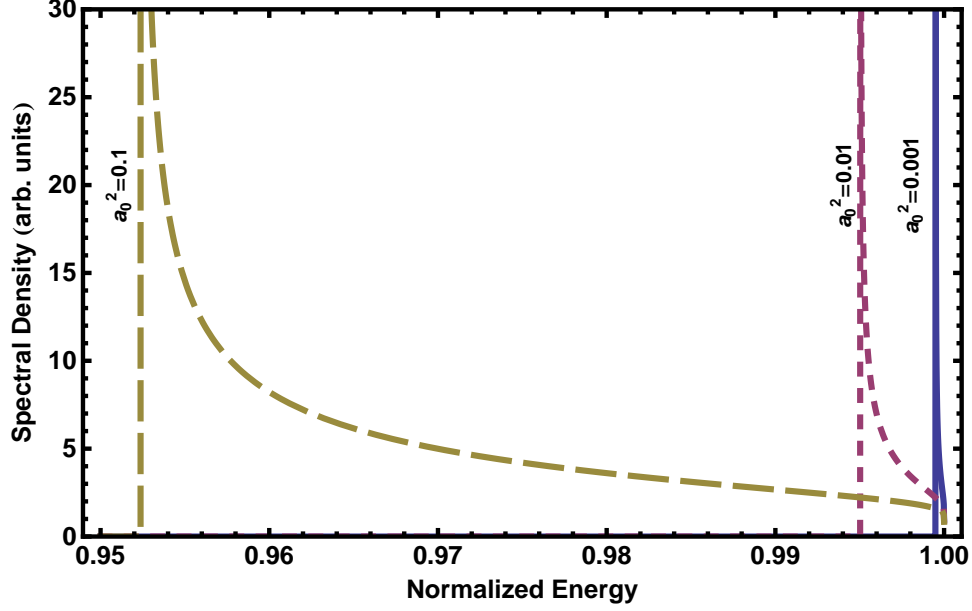


Figure 15: Spectrum as a function of peak photon density (parameterized by a_0^2)

We can add in the electron focusing effects as well by making our electron in the integral not a single electron but representative of the density of the electrons. The number of scattered electrons then scales linearly with the electron density n_e , which depends on the longitudinal position of the bunch through

$$\beta_0 = \frac{\beta \gamma \sigma_0^2}{\epsilon_n} \quad \sigma(z) = \sigma_0 \sqrt{1 + \left(\frac{z}{\beta_0}\right)^2}$$

where γ is the electron relativistic factor, σ_0 is the rms electron beam size at the focus, and ϵ_n is the normalized emittance. Thus

$$n_e(z) \propto \left(\frac{\sigma_0}{\sigma(z)}\right)^2.$$

Adding this factor to the integral now gives

$$\begin{aligned} N_s(E_0, w_0, \tau) &\propto \int_{-\infty}^{\infty} \left(\frac{\sigma_0}{\sigma(z)}\right)^2 \mathbf{S}(0, 0, -ct, t) \cdot \hat{z} dt \\ &= \frac{E_0^2 \pi z_r \beta_0}{2c^2 \mu_0 (\beta_0^2 - z_r^2)} \left[\beta_0 e^{\frac{8z_r^2}{c^2 \tau^2}} \left(1 - \operatorname{erf} \frac{2\sqrt{2}z_r}{c\tau}\right) - z_r e^{\frac{8\beta_0^2}{c^2 \tau^2}} \left(1 - \operatorname{erf} \frac{2\sqrt{2}\beta_0}{c\tau}\right) \right] \end{aligned}$$

when $\beta_0 \neq z_r$, or

$$N_s(E_0, w_0, \tau) \propto \frac{E_0^2 \pi}{4c^2 \mu_0} \left[\frac{4z_r}{c\tau} \sqrt{\frac{2}{\pi}} + e^{\frac{8z_r^2}{c^2 \tau^2}} \left(1 - \frac{16z_r^2}{c^2 \tau^2}\right) \left(1 - \operatorname{erf} \frac{2\sqrt{2}z_r}{c\tau}\right) \right]$$

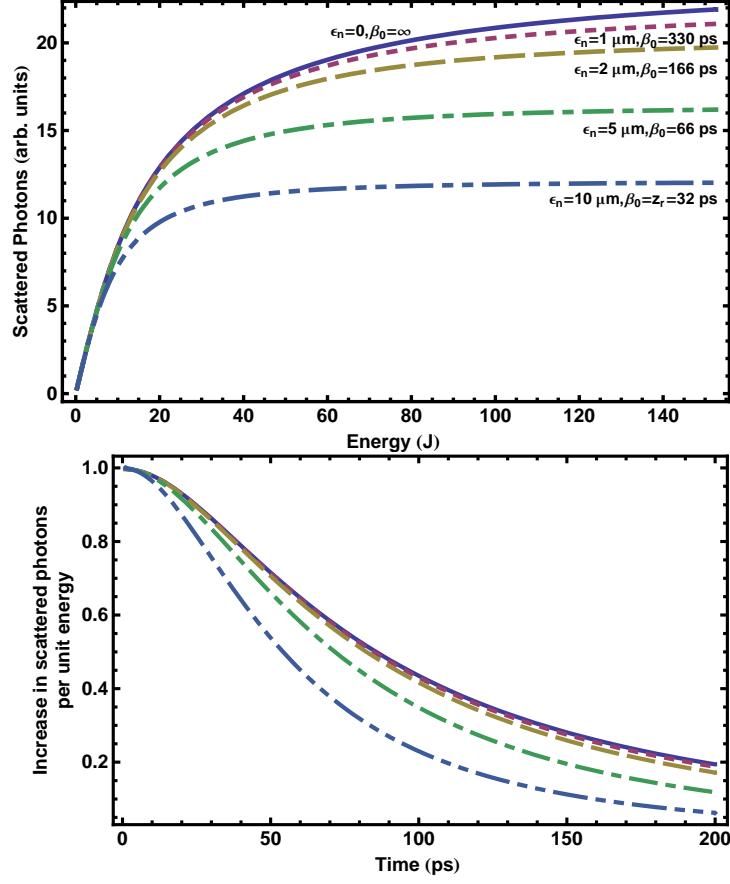


Figure 16: Top: Scattered photon flux versus laser energy, holding the peak a_0 constant and adjusting the laser pulse length. Normalized to be 1 at 1 J ($\tau \approx 7$ ps). Bottom: Marginal increase in scattered gammas as the pulse length is increased (derivative with respect to τ of the top figure).

when $\beta_0 = z_r$.

Figure 16 shows these equations plotted for the specific values of $\gamma = 250$, $w_0 = 2\sigma_0 = 40 \mu\text{m}$, and $\lambda = 532 \text{ nm}$, which give $z_r = 32 \text{ ps}$. A variety of ϵ_n are plotted to give a sense of the effect of the electron focusing. The upper plot is parameterized by the laser energy, which given the a_0^2 limit of 0.001 is proportional to pulse length. It shows there is a limit to how much energy can be used in a single pulse to generate gamma rays. The lower plot shows the (normalized) number of additional photons generated per additional unit of incident laser energy (or pulse length), showing that after a few tens of ps the (relatively expensive) laser photons generate less and less gamma rays at the margin.

Based on this analysis, the optimal driving laser for a Compton source has an $a_0^2 \approx 0.001$ with a pulse length of a few 10s of ps, leading to ideal interaction energies on the order of a few Joules per pulse.

3.2 Physical Systems

Having decided on the optimal parameter space, we can examine the current state of the art for lasers in this regime. Fig. 17 shows the results of a survey of the literature. Plotted are reported lasers with repetition rate on the x -axis and pulse energy on the y -axis. A wide range of laser systems are shown. In general, the systems on the left part of the graph (high energy, low rep-rate) are bulk optical systems (Nd:YAG or Nd:YLF slabs, for example), while on the right part (low energy, high rep-rate) are fiber-based laser systems. Also shown on the graph are lines indicating the average power (energy per pulse \times pulses per second) of the lasers. The graph further indicates the regions where a 10 ps pulse starts to reach an a_0^2 value large enough to compromise the gamma ray beam's spectral quality, and a rough estimate of the number of photons that would be scattered per shot from a 1 nC, 1 mm mrad, 20 μ m, 10 ps electron beam interacting with the laser pulse.

3.2.1 Single Pulse Limitations

A quick glance at the reported lasers show that the current state of the art is approximately 100 W average power running continuously, limited largely by engineering issues involved with thermal management of the waste heat generated and the current price of diode pump lasers. A detailed analysis of fiber laser technology[36] shows that 36 kW is a theoretical maximum power for single fiber lasers, regardless of the mode size in the fiber. There is also a limit of several mJ in total energy due to nonlinear refractive index effects in the fiber material. There are ways to overcome this by stacking multiple fiber outputs together either coherently to increase the per-pulse energy, which is a technical challenge that hasn't fully been resolved, or incoherently with a time delay to increase the rep-rate. These systems operate quite well in the 10s of kHz to few GHz regime, and could be useful solutions for superconducting-linac-based scattering systems.

Most of the high-energy, high-power lasers that have been reported have been ns-scale lasers (indicated by squares in Fig. 17). This is because the materials used have been narrow (< 1 nm) bandwidth materials, which makes the application of chirped-pulse amplification (CPA) difficult because a standard compressor would require 30 m of effective grating separation to get the necessary dispersion. However, LLNL developed technology, the Hyperdispersion Stretcher and Compressor, makes CPA practical with these systems, allowing the necessary compressor to fit on a 10 ft table comfortably. This technology has been demonstrated in the T-REX project, which produced a 10 Hz, 800 mJ, 10 ps laser pulse. Thus all these systems could be turned into ps-scale systems. It can be seen that these systems fall in the same 10-1000 W range presently. The Mercury laser architecture is expected, if the aperture size were scaled from the current 3×5 cm aperture to a 20×30 cm aperture, to be able to produce 42 kW of average power. A design exists, using the technology built for Mercury, to produce a tabletop 10 J, 120 Hz laser system, but it has not yet been tested. Currently, a 1 J, 120 Hz system is being built for the Velociraptor project (the follow-up to the T-REX project).

3.2.2 Multiple Pulse Solutions

One simple way to arbitrarily increase the available laser energy at the interaction point is by building multiple copies of the laser. Building two copies of the T-REX interaction laser would

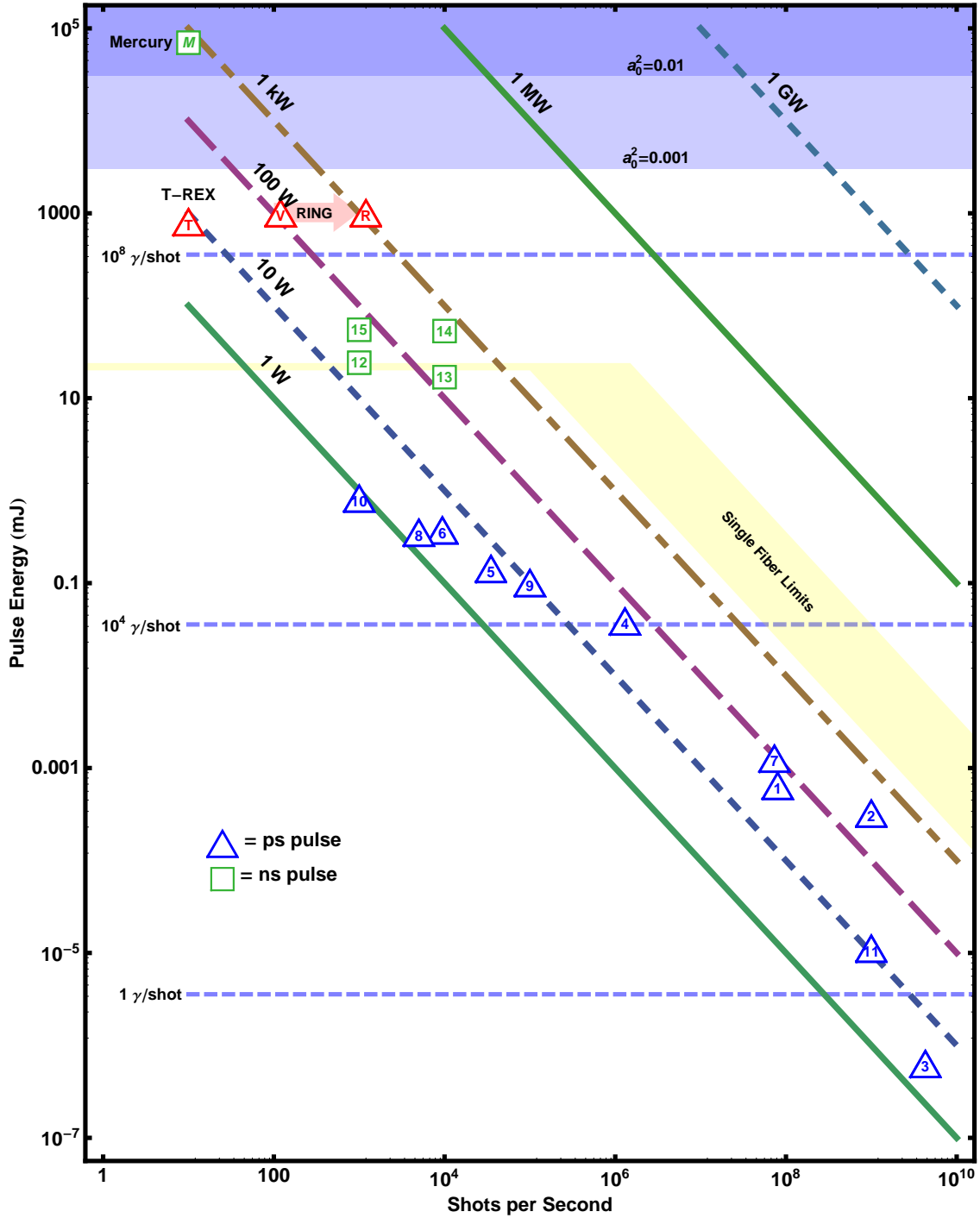


Figure 17: Plot showing the performance of recently reported ps- and ns-scale lasers as a function of repetition rate and pulse energy. Numbers 1-15 correspond to Refs. [21, 22, 23, 24, 25, 26, 27, 28, 29, 30, 31, 32, 33, 34, 35]. The limits for single-fiber scaling come from Ref. [36]. Also indicated are regions where $a_0^2 = 0.001$ and 0.01 and the energies at which an optimal 1 nC electron bunch would scatter 1, 10^4 , and 10^8 photons per shot. The lettered points are: T-T-REX performance, V-planned Velociraptor performance with DNDO funded laser upgrade, R-enhancement of Velociraptor possible with recirculation, M-LLNL's Mercury laser performance

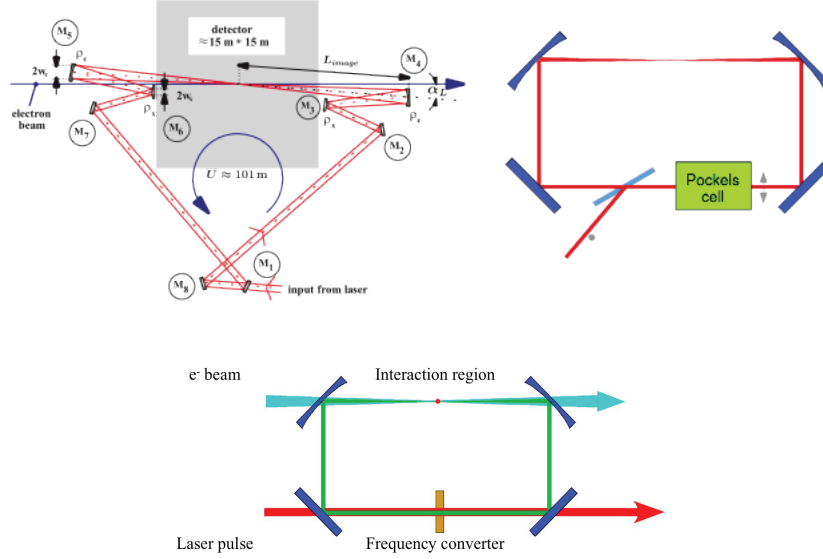


Figure 18: Pulse recirculation options. Upper left: Cavity enhancement geometry (TESLA design). Upper right: cavity optical switch. Lower: nonlinear gating cavity.

allow the same energy per pulse with twice as many pulses. This could, to some degree, even be done for less than twice the cost, since the preamps, stretcher, and compressor hardware could be used by both systems. In this simple case, any rep-rate could be reached by building enough interleaved laser systems. There is a more sophisticated solution as well. A 1 J laser pulse scattering off an optimal 1 nC electron bunch can generate 10^8 photons/shot. A 1 J, 532 nm laser has

$$\frac{E_l}{\frac{hc}{\lambda}} = 2.6 \times 10^{18} \text{ photons},$$

meaning that after the scattering we are left with $10^{18} - 10^8 = 10^{18}$ unused photons. Collecting these photons and sending them through the interaction region again would effectively increase the average power of the interaction laser with no extra power required.

There are a few different ways to implement this recirculation, illustrated in Fig. 18. The first is the resonant cavity enhancement scheme. In this system, a series of pulses are continuously fed into a recirculating cavity, allowing several consecutive pulses to add coherently and generate a much higher intracavity power. Laser enhancement factors of 1000 or more have been reported using this scheme [37, 38]. These systems are inherently limited to high-rep rate driving lasers, because the intracavity path length is on the order of a few feet (= a few ns). Since this scheme relies on stacking consecutive pulses to realize the enhancement, subsequent pulses must arrive before the first pulse has dissipated, which will generally take on the order of 100s of ns to a few μ s based on cavity losses. For a lower rep-rate ($< \text{MHz}$) laser this scheme does not offer significant advantages. The additive nature of the system also requires that the cavity length be interferometrically stable ($< 100 \text{ nm}$ path length change) to produce the desired enhancement: a difficult goal, but one that has been well demonstrated.

The alternative scheme is to use an optical switch in the cavity. In order to maintain

significant energy for several round trips, the mirror losses in the cavity must be very small, which then necessitates a scheme to get light into the cavity (for the resonant cavity case above, this is not a significant issue, and it manifests itself as a “build-up time” needed to reach the desired enhancement level). One common switch is an electrooptic pockels cell, which can rotate the polarization of the laser pulse at any given time. This allows a polarizer to be used as the means to couple the light into the cavity. This scheme has been studied in both a passive mode[39] and in an active mode with a gain medium to replenish lost energy on each round trip[40]. The main difficulty of this architecture is that the electrooptic crystal is necessarily thick to get the needed 90° polarization rotation, and necessarily small in diameter to get the proper electric field over the whole crystal aperture. This crystal must also be transited at high intensity on each pass through the cavity. While this might work for low energy (≤ 1 mJ) systems, for Joule-level pulses the nonlinear optical effects in the pockels cell will lead to degradation of the lasers spectrum and wavefront, precluding the tight, consistent focusing needed to successfully scatter off the electron beam.

Instead of using optical polarization as the switching mechanism, a system pioneered at LLNL has demonstrated the effectiveness of changing the laser wavelength to switch the pulse into the cavity. In this design (called RING: Recirculation Injection by Nonlinear Gating), a relatively thin, large aperture nonlinear crystal is used which doubles the frequency of 1064 nm light to produce 532 nm light. The mirrors of the cavity are dielectrically coated to be highly reflective at 532 nm, and highly transmissive at 1064 nm. This allows the light to enter the cavity, change frequency, and then be trapped. There is much less material for the beam to pass through, and the beam can be much larger when it passes through the crystal, so there will be significantly less accumulation of nonlinear distortion. Initial demonstrations with both a 0.5 mJ pulse showing $49\times$ gain and an 180 mJ pulse showing $14\times$ gain have been performed[41].

3.3 Laser Summary

For the design of a minimal-bandwidth Compton scattering source, a 10 ps, 1-10 J class laser presents the optimal compromise between efficiency and flux. Currently designed systems (soon to be demonstrated) can produce around 1 kW of average power, which when coupled with the desired repetition rate sets the energy that can be delivered to the interaction point. Increasing beyond that kW level is a function of the maturation of the pump diode market, lowering the currently prohibitive cost of adding more pump power to the system, and solving thermal engineering issues. These are issues that are currently being addressed by a variety of research areas, from the power-plant incarnation of inertial confinement fusion which requires 100s of kJ at 10 Hz (MW class) to the laser power needed to implement a 1 TeV scale laser wakefield accelerator (10s of MW) for high energy physics research.

The cheat that is available in the Compton-scattering application is that most of the photons don’t get scattered and can be recirculated. The most viable option for doing this on the Joule scale is the RING system recently demonstrated to increase the number of photons available at the interaction point by at least a factor of 14. This scheme however does place a burden on the electron beam system: the interpulse spacing in one of these cavities is on the order of a few to 10s of ns. Thus the electron beam needs to either be running at 10s to 100s of MHz to collide with each laser pass, or the accelerator has to run in a “microbunch” mode,

where several bunches come with ns spacing at a lower (e.g. <kHz) rep rate. In either case, the close spacing of the bunches requires careful attention to interbunch interaction via cavity wakefields in the accelerating structure, which can compromise the delivered electron quality.

Acknowledgment

This work was supported by the Domestic Nuclear Detection Office of the Department of Homeland Security and performed under the auspices of the U.S. Department of Energy by Lawrence Livermore National Laboratory under Contract DE-AC52-07NA27344.

References

- [1] W. J. Brown and F. V. Hartemann, Phys. Rev. ST Accel. Beams **7**, 060703 (2004).
- [2] P. B. Wilson, Tech. Rep. SLAC-PUB-7449, Stanford Linear Accelerator Center (1997).
- [3] W. D. Kilpatrick, Rev. Sci. Inst. **28** (1957).
- [4] J. W. Wang, Tech. Rep. SLAC-AP-51, Stanford Linear Accelerator Center (1986).
- [5] J. W. Wang and G. A. Loew, in *1989 Particle Accelerator Conference* (IEEE, 1989), p. 1137.
- [6] J. W. Wang and G. A. Loew, Tech. Rep. SLAC-PUB-7684, Stanford Linear Accelerator Center (1997).
- [7] S. Döbert, in *Proceedings of LINAC2002* (IEEE, 2002), p. 274.
- [8] K. J. Kim, Nucl. Instrum. Methods Phys. Res., Sect. A **275**, 201 (1989).
- [9] J. Rosenzweig and E. Colby, in *Advanced Accelerator Concepts: 6th Workshop* (AIP Conference Proceedings, 1995), vol. 335, p. 724.
- [10] A. E. Vlieks, G. Caryotakis, C. DeStefano, J. P. Heritage, E. Landahl, N. C. Luhmann, D. Martin, and A. Menegat, in *High Energy Density and High Power RF: 6th Workshop* (AIP Conference Proceedings, 2003), vol. 691, p. 358.
- [11] S. G. Anderson, C. P. J. Barty, D. J. Gibson, F. V. Hartemann, M. Messerly, M. Shverdin, C. W. Siders, A. M. Tremaine, H. Badakov, P. Frigola, et al., in *Proceedings of PAC07* (IEEE, 2007), p. 1242.
- [12] F. J. Sacherer, IEEE Trans. Nucl. Sci. **18**, 1105 (1971).
- [13] J. B. Rosenzweig and L. Serafini, Phys. Rev. E **49**, 1599 (1993).
- [14] S. G. Anderson and J. B. Rosenzweig, Phys. Rev. ST Accel. Beams **3**, 094201 (2000).
- [15] L. Young and J. Billen, Tech. Rep. LA-UR-96-1835, Los Alamos National Laboratory (1996).

- [16] M. Ferrario, J. E. Clendenin, D. T. Palmer, J. B. Rosenzweig, and L. Serafini, in *Proceedings of the ICFA Advanced Accelerator Workshop on the Physics of High Brightness Beams, Los Angeles, 1999*, edited by J. B. Rosenzweig and L. Serafini (World Scientific, Singapore, 2000), p. 534.
- [17] L. Serafini and J. B. Rosenzweig, Phys. Rev. E **55**, 7565 (1997).
- [18] D. Attwood, *Soft X-Rays and Extreme Ultraviolet Radiation* (Cambridge University Press, Cambridge, 1999).
- [19] A. E. Siegman, *Lasers* (University Science Books, Sausalito, CA, 1986).
- [20] G. B. Arfken and H. J. Weber, *Mathematical Methods for Physicists* (Academic Press, San Diego, CA, 1995), 4th ed.
- [21] J. Limpert, A. Liem, T. Gabler, H. Zellmer, and A. Tunnermann, Opt. Lett. **26**, 1849 (2001).
- [22] P. Dupriez, A. Piper, A. Malinowski, J. K. Sahu, M. Ibsen, Y. Jeong, L. M. Hickey, M. N. Zervas, J. Nilsson, and D. J. Richardson, in *Optical Fiber Communication Conference and Exposition and The National Fiber Optic Engineers Conference* (Optical Society of America, 2005), p. PDP3.
- [23] H. Fuchs, M. A. Tremont, O. Casel, D. Woll, T. Ulm, J. A. L'Huillier, and R. Wallenstein, Appl. Phys. B **87**, 425 (2007).
- [24] B. Luther-Davies, V. Z. Koley, M. J. Lederer, N. R. Madsen, A. V. Rode, J. Gieseke, K.-M. Du, and M. Duering, Appl. Phys. A **79**, 1051 (2004).
- [25] M. Siebold, J. Hein, R. Sauerbrey, T. Bergmann, and G. Hollemann, in *2003 Conference on Laser and Electro-Optics Europe* (IEEE, 2003), pp. 33 (Paper CA7-1-WED).
- [26] S.-X. Xu, X.-Y. Wei, K.-M. Du, and J.-Z. Li, Chin. Phys. Lett. **25**, 2521 (2008).
- [27] R. Peng, L. Guo, X. Zhang, F. Li, Q. Cui, Y. Bo, Q. Peng, D. Cui, and Z. Xu, Opt. Comm. **281**, 2879 (2008).
- [28] M. Siebold, M. Hornung, J. Hein, G. Paunescu, R. Sauerbrey, T. Bergmann, and G. Hollemann, Appl. Phys. B **78**, 287 (2004).
- [29] T. Herrmann, B. Klimt, and F. Siegel, Industrial Laser Solutions for Manufacturing **October** (2004), URL http://www.industrial-lasers.com/display_article/214378/39/none/none/Feat/Micromachining-with-picosecond-laser-pulses.
- [30] M. Hornung, M. Siebold, J. Hein, R. Sauerbrey, and G. Hollemann, in *Advanced Solid-State Photonics* (Optical Society of America, 2005), p. MF2.
- [31] A. Piper, A. Malinowski, B. Thomsen, D. J. Richardson, L. M. B. Hickey, and M. N. Zervas, in *Conference on Lasers and Electro-Optics/Quantum Electronics and Laser Science and Photonic Applications Systems Technologies* (Optical Society of America, 2005), p. CTuCC3.
- [32] D. Li, Z. Ma, R. Haas, A. Schell, P. Zhu, P. Shi, , and K. Du, Opt. Lett. **33**, 1708 (2008).

- [33] P. Zhu, D. Li, B. Qi, A. Schell, P. Shi, C. Haas, S. Fu, N. Wu, and K. Du, *Opt. Lett.* **33**, 2248 (2008).
- [34] E. C. Honea, R. J. Beach, S. C. Mitchell, J. A. Skidmore, M. A. Emanuel, S. B. Sutton, and S. A. Payne, *Opt. Lett.* **25**, 805 (2000).
- [35] Y. Isyanova and P. F. Moulton, in *Conference on Lasers and Electro-Optics/Quantum Electronics and Laser Science Conference and Photonic Applications Systems Technologies* (Optical Society of America, 2007), p. CTuD7.
- [36] J. W. Dawson, M. J. Messerly, R. J. Beach, M. Y. Shverdin, E. A. Stappaerts, A. K. Sridharan, P. H. Pax, J. E. Heebner, C. W. Siders, and C. Barty, *Opt. Exp.* **16**, 13240 (2008).
- [37] C. Gohle, T. Udem, M. Herrmann, J. Rauschenberger, R. Holzwarth, H. A. Schuessler, F. Krausz, and T. W. Hansch, *Nature* **436**, 234 (2005).
- [38] R. J. Jones, K. D. Moll, M. J. Thorpe, and J. Ye, *Phys. Rev. Lett.* **94**, 193201 (2005).
- [39] T. Mohameda, G. Andlerb, and R. Schuch, *Opt. Commun.* **214**, 291 (2002).
- [40] D. Yu and B. Stuart, in *Proceedings of the 1997 Particle Accelerator Conference* (IEEE, 1997), p. 3V030.
- [41] M. Y. Shverdin, F. Albert, S. G. Anderson, S. M. Betts, D. J. Gibson, F. V. Hartemann, M. J. Messerly, V. A. Semenov, D. P. McNabb, C. W. Siders, et al., in *Nonlinear Optics: Materials, Fundamentals, and Applications* (Optical Society of America, 2009), p. NThC4 (forthcoming).